Mercury Impact Ejecta's Contribution to its Own Meteoroid Population

by

Pierce M. Jackson

A thesis submitted to the Graduate Faculty of
Auburn University
in partial fulfillment of the
requirements for the Degree of
Master of Science

Auburn, Alabama
May 7, 2022

Keywords: Mercury (planet), Impact processes, Ejecta, Meteoroids, Micrometeoroids, Dust, Regolith, Orbits, Planetary Science

Approved by

Masatoshi Hirabayashi, Chair, Assistant Professor of Aerospace Engineering
Dennis Bodewits, Associate Professor of Physics
Davide Guzzetti, Assistant Professor of Aerospace Engineering

Abstract

Mercury's position in the inner Solar System and lack of an atmosphere subjects it to the greatest mean velocity impacts of the inner Solar System. Ejecta launched at speeds less than 4.25 km s^{-1} are retained by the planet and contribute to Mercury's dust environment, secondary crater population, or regolith gardening. However, simple-crater forming impact events can accelerate regolith to velocities high enough to escape Mercury's Hill sphere, some of which may eventually come back to Mercury. It is not well understood how much of this ejected material returns to Mercury. This thesis seeks to understand how much of Mercury's meteoroid population is composed of material originating from itself.

A host of impacts into Mercury's surface are simulated using the ejecta-scaling relationships of Housen & Holsapple (2011) [17] and Richardson et al. (2007) [32]. Properties of launched particles are such as ejection speed and direction are quantified so their trajectories can be calculated. Ejecta that escapes Mercury have their orbital trajectories propagated by an N-body code for thousands of years under the influence of gravity, solar radiation pressure, and Poynting-Robertson drag. They are monitored for entering a planet's Hill sphere or approaching too close to the Sun.

The likelihood of a particle returning to Mercury is dependent on its size (or rather, its value of β, the ratio of radiation force to solar gravity). Only 22% of 10 μm radius particles come back because of their susceptibility to spiralling into the Sun due to the decelerating effects of Poynting-Robertson drag. On the other hand, grains with radii of 50, 100, 500, and 1000 μm are not as readily perturbed by non-gravitational forces. The percentages of these particles that return to Mercury are approximately 50.5%, 68.7%, 85.7%, and 88.6%, respectively.

Consequently, it is estimated that 39% of particles and 87% of mass that escapes Mercury via an impact event will return within 10,000 years. Grains with radii on the order of 10s of micron, by number, contribute about 80% of returning particles but only 0.2% of returned mass.

Alternatively, particles with radii greater than a few hundreds of micron compose less than 20% of returning particles, but over 99.5% of the returning mass. These results imply that Mercury's meteoroid population is almost certainly is composed partially of material originating from itself and that unhindered grains will re-impact Mercury's surface and further contribute to surface processes such as boulder decimation, regolith breakup and gardening, melt production, volatile vaporization and topographic diffusion.

Acknowledgments

I first and foremost want to acknowledge the unconditional love and support from my family. They cheered me on during the highs and encouraged me through the lows and, honestly, I am not sure where I would be without all that they have done for me. Mom, Dad, and Caroline (can't forget Chonk 1 and Chonk 2), I love you. My office-mates allowed me to feel human and understood. They also kept me sane in the wake of completing the first year of this degree during the COVID-19 lockdown. Ryota, Yaeji, Joe, Nick, Jack, Keziban, Skyler, Lauren, Pedro, Hephzibah, Praveen, and Sam (and the other in 154)- cheers. Thanks to coffee. I drink a lot of coffee now (I did anyway, but still). Thanks to Dr. Thurow for allowing me to join the department (after the application deadline had passed...) Thanks to Dr. Bodewits, not only for being on my advising committee, but all the knowledge and support he has shared with me since joining the Physics department. Thanks to Dr. Guzzetti for his willingness to participate on the advising committee as well. Finally, thank you to Dr. Toshi for allowing me this opportunity. I can, without a doubt, say that I have become a more independent and thorough researcher over the course of this degree.

Table of Contents

Abstract ii

Acknowledgments iv

1 Introduction 1

1.1 Research Background 1

1.1.1 Projectile Definitions 2

1.1.2 Mercury's Meteoroid Environment 3

1.1.3 Meteoroids' Influence on Mercury's Surface 5

1.2 Research Goal and Outlines 7

2 Understanding Impacts 8

2.1 Regolith/Surface 9

2.2 The Cratering Process 10

3 Modeling Impacts and their Ejecta 13

3.1 Impact Dynamics Model 13

3.1.1 Particle Ejection Speed as a Function of Position 14

3.1.2 Crater Radius in the Gravity Regime 17

3.1.3 Final Particle Ejection Speed Model for Impacts Normal to Surface . . 18

3.1.4 Particle Ejection Angles, Directions, and Adjustments to Velocity for Oblique Impacts 20

3.1.5 Amount of Mass Ejected 22

3.2 Target Properties 23

3.3 Orbit Propagation Model 27

4 The Simulations 30

4.1 Code Validation 30

4.2 Impact-Event Setup 30

4.3 N-Body Code 36

5 Results 41

5.1 10 µm 42

5.2 50 µm 43

5.3 100 µm 44

5.4 500 µm 46

5.5 1000 µm 48

5.6 Composite Case 50

6 Discussion & Conclusions 59

6.1 Discussion of Results 59

6.1.1 To Return, or Not to Return? 59

6.1.2 Mass Return 61

6.2 Potential Improvements and Future Work 65

6.3 Conclusion 66

References 69

List of Figures

3.1 Figure 3 from Liu & Schmidt (2018) [23] showing the Mie theory calculations of radiation pressure efficiency, Q_{pr} for different particle sizes. Grains are considered to be silicate. Liu & Schmidt, A&A, 609, A57, 2018, reproduced with permission ©ESO. 28

4.1 Recreation of Figure 13 from [17]. Particle ejection speed versus radial launch position in terms of impactor properties. 31

4.2 Recreation of Figure 14 from [17]. Particle ejection speed versus radial launch position in terms of crater radius for gravity-dominated impacts. 31

4.3 Recreation of Figure 16 from [17]. Mass ejected at a speed greater than v in terms of impactor properties. 32

4.4 Schematic of impact simulation. N = 12 ejecta layers are rotated (not depicted) around the impact point with particles ejected every 10 degrees. This gives 432 particles per individual impact scenario. No material is ejected from the surface within the 'compaction zone.' Particles from this region, however, are pushed out and follow streamlines [24] to be ejected from the surface at greater distances from the impact. 33

4.5 Minimum combination of impactor speed and size that will eject particles at a speed equal to Mercury's escape velocity. 35

4.6 Impact Code flowchart 36

4.7 Ejecta from an oblique, gravity-dominated impact with parameters: $a_i = 10$m, $\phi = 30^o$, impacting at 45^oS, 90^oE on Mercury's surface with $-x$ being the downrange direction. 37

4.8 Propagation of a single, medium category, ejecta layer (36 particles) from the same impact as Fig.(4.7) for 36 days. 40

5.1 Results of 3024 test particles with radius 10 μm propagated for 5000 years. . . . 43

5.2 Example of 4 ejected particles taking trajectories from Mercury into the Sun. . . 44

5.3 Results of 3024 test particles with radius 50 μm propagated for 5000 years. . . . 45

5.4 Results of 3024 test particles with radius 100 μm propagated for 5000 years. . . 46

5.5 Example trajectory of particle leaving and returning to Mercury. 47

5.6 Results of 3024 test particles with radius 500 μm propagated for 5000 years. . . 48

5.7 Results of 3024 test particles with radius 1000 μm propagated for 5000 years. . 49

5.8 The heliocentric distances of all the particles that were not intercepted by the simulations of Sections 5.1-5.5 at the end of the 5000 years of propagation. A majority of the remaining (non-intercepted) particles have stayed at or inside of Mercury's orbit. The peak occurs close to 0.39 AU, the average orbital distance of Mercury. Some particles have moved beyond 1 AU and further into the outer Solar System. Particles that have a heliocentric distance larger than 50 AU are considered to have exited the Solar System. They are represented by the bin at 50 AU. 50

5.9 Trends of intercepted particles based on size 54

5.10 Composite result: Total number of particles intercepted and returned to Mercury 55

5.11 Composite result: particle time-to-capture vs. ejection speed 56

5.12 Composite result: particle relative interception velocity vs. launch speed from impact 57

5.13 Composite result: particle relative interception velocity vs. time-to-capture . . . 58

List of Tables

3.1 Scaling laws used to simulate gravity-dominated impacts and the resulting ejection velocities 24

3.2 Scaling laws used to simulate strength-dominated impacts and the resulting ejection velocities 25

3.3 Target properties used in impact simulations 26

4.1 Impactor properties used in impact simulations 34

4.2 Hill sphere radii of relevant Solar System bodies. 39

5.1 Results of composite simulation by particle size. The specific fraction refers to the portion of particles of that size that that returned to Mercury (column 4 / column 2). The total fraction is that size's contribution to the total number of particles that returned to Mercury (column 4 / 38,403). 52

5.2 Summary of the results of the individual particle size simulations and the composite simulation. Percentage of intercepted particles are with respect to the total number in the simulation. Avg. Time refers to the average amount of time after ejection that particles took to be captured by the body. Impact speed is found by accelerating particles down to the surface of Mercury with an initial velocity equal to the velocity at which the particle crossed into the Hill sphere. . 53

6.1 β and τ_{pr} for various particle sizes 62

6.2 Fractional makeup of the total ejected mass (F_r) and the fraction of particles of that specific size that return to Mercury (S_{fr}) 64

Chapter 1

Introduction

1.1 Research Background

Meteorite impacts are a dominant surface process on Mercury. They accelerate regolith formation through the destruction of boulders and drive operations such as regolith gardening, topographic diffusion, and the release of volatiles which contribute to the planet's exosphere. In addition, Mercury has lacked major geologic activity over the last ~ 3.5 billion years [25, 47, 48]. This means that most of the other processes that influence a planet's surface (such as volcanism, tectonics, and seismic activity) are not present, allowing for bombardment by meteorites and micrometeorites, alike, to assume a unique role in shaping Mercury's surface [5, 49, 53, 54, 55] and exosphere [50, 51, 52].

Mercury's position close to the Sun subjects it to high velocity impacts from a wide population of impactors, large and small. Both asteroids and comets often follow orbits with perihelion near or within Mercury's orbit. This not only means that these objects themselves might be intercepted by Mercury, but auxiliary material such as meteoroids and dust can also be accreted by the planet [4, 30, 2, 1]. The lack of an atmosphere or any moons means that nearly all such material that is captured by Mercury will eventually make its way to the surface resulting in one of the highest cratering rates in the inner Solar System [20, 21].

The combination of high velocity impacts, high cratering rate, the lack of an atmosphere, and low surface gravity (3.7 m s^{-2}) make it likely that surface material is readily launched off the planet via impacts. As a result, it is probable that some portion of this material contributes to Mercury's own meteoroid environment, though how much is currently unknown. Given the

important role of meteorites to its surface and exosphere, this work seeks to better understand how material originating from Mercury contributes to its own meteoroid population.

The rest of this chapter will discuss the meteoroid environment around Mercury as it is currently understood and the role this material plays in influencing surface properties.

1.1.1 Projectile Definitions

The precise definition of 'meteoroid' and 'micrometeoroid' are sometimes ambiguous. It is widely accepted that the term 'meteoroid' refers to a small, naturally occurring, solid body that is not large enough to be considered an asteroid or comet [9]. The ambiguity arises from the exact meaning of the descriptor 'small.' For example, Pokornỳ et al. (2018) [30] investigates particles with radii below 0.1 cm and exclusively refers to them as 'meteoroids;' Vaniman et al. (1991) [9] describes particles with diameter smaller than 0.1 cm as 'micrometeoroids;' Domingue et al. (2014) [5] and Borin et al. (2009, 2016) [2, 1] describe particles with radii below 1 cm as 'micrometeoroid' (smaller than 1 mm as 'dust'); and Marchi et al. (2005) [56] is more of an anomaly, considering particles with radii of $1 - 10^4$ cm in their analysis of 'meteoroid' flux at Mercury. In practice, the ambiguity in the definition between the two is not a problem. These particles (smaller that 1 cm) are small enough that their orbital motion can be perturbed by non-gravitational forces such as Poynting-Robertson drag and solar-radiation pressure and they will not produce significantly large craters upon impact. The precise definition of 'meteoroid,' however, becomes important in the scope of this manuscript because these are the objects on which we are focused.

In this text, the nomenclature of [13] will be adopted: a 'meteoroid' will have a diameter between 10µm - 1m. 'Micrometeoroids' are contained within this definition and have diameters from 10µm - 2mm. The terms 'micrometeoroid' and 'dust' will be used interchangeably - they refer to the smallest meteoroids.

The term 'impactor' will also be used often. This will refer to objects larger than the chosen definition of meteoroids that are capable of producing craters with significant amounts of ejecta. That is, for example, objects with diameters greater than ~ 5m. Unlike with meteoroids, this chosen definition of 'impactor' is not necessarily meant to be rigorous, but rather provide a

distinction between objects that are generated via impacts or mechanical perturbations (i.e. meteoroids; whether launched into space by an impact on a planetary surface, collisional breakup in space, outgassing of comets, rotational instability of small bodies, etc...) and objects that produce significantly large craters with ejecta that are capable of becoming meteoroids.

1.1.2 Mercury's Meteoroid Environment

Meteoroids bombarding Mercury originate from four primary sources: asteroids from the main asteroid belt (main-belt asteroids; MBA), Jupiter-family comets (JFC), Halley-type comets (HTC), and Oort Cloud comets (OCC) [30]. Jupiter-family comets are classified as short-period comets, have orbital periods 20 years or less, relatively low inclinations, and as their name implies, have aphelion near or within the orbit of Jupiter. Halley-type comets are another classification of short-period comets, have periods between 20 - 200 years, and can have inclinations greater than 90°. Oort Cloud comets are designated as long-period comets because their orbits exceed 200 years and can extend to upwards of millions of years. HTC and OCC orbits are often highly eccentric and inclined, sometimes leading to retrograde motion around the Sun [58, 59].

Analytical methods by Cintala (1992) [4] and numerical simulations by Borin et al. (2009, 2016) [2, 1], Pokornỳ et al. (2018, 2021) [30, 53], and Marchi et al. (2005) [56] (among others) have provided much insight into the meteoroid population falling onto Mercury. Material originating from MBA, JFC, HTC & OCC are understood to compose nearly all of the meteoroid population, with a majority coming from JFC. Estimates averaged over the whole of Mercury's orbit gives $\sim 12.16 \pm 5.57$ tons of meteoroid mass accreted per day and over half of it ($\sim 7.84 \pm 3.13$ tons) is from JFC [30]. While the precise value varies between studies, it is generally accepted that the meteoroid flux at Mercury is a few times higher than on the lunar surface. Numerical simulations by Le Feuvre & Wieczorek (2008) [20] indicate that the average impact flux is ~ 2 times higher and the average cratering rate is $\sim 2.6 - 3.6$ (for impactors with $d > 1$ km and $d > 20$ km, respectively) higher for Mercury relative to the Moon. These impactors also have the greatest mean approach velocity (42.2 km s^{-1}) and impact velocity (42.5 km s^{-1}) of the inner Solar System; both over 2 times greater than at the Moon.

Mercury's eccentric orbit, as well as its asynchronous 3:2 orbital resonance with the Sun, results in a distinct diurnal (morning vs. evening) asymmetry in impact direction and impact rate. Marchi et al. (2005) [56] finds that, on average, impacts are more frequent during the planet's *a.m.* than *p.m.*, except for particles with radius $r < 13$ cm. Ultimately, this is due to larger particles having longer collisional lifetimes than small particles. They explain:

> The increase of the *am/pm* ratio with collisional lifetime is normal, as already pointed out by Morbidelli & Gladman (1998) [69]. It is due to the fact that the longer the collisional lifetime, the more numerous are the meteoroids with small semi-major axis, which typically tend to fall on the morning hemisphere. Also, it is normal that the *am/pm* ratio is larger for Mercury at perihelion, because the orbital velocity of the planet is higher, and the planet tends to catch up the meteoroids, rather than being caught up by them. [56]

Impact velocity will also vary depending on the object's size (i.e. whether it is a 'meteoroid' or an 'impactor') and origin. Meteoroids from long-period comets (HTC & OCC) can extend to over 100 km s^{-1} due to their ability to follow retrograde orbits. Borin et al. (2009) [2] focused on dust particles from MBAs and found an average impact velocity of 17 km s^{-1}, which is similar to Cintala (1992)'s [4] findings of 20.5 km s^{-1}. Pokornỳ et al. (2018) [30] found that meteoroids from MBA and JFC can reach up to 70 km s^{-1} at perihelion and 50 km s^{-1} at aphelion. However, their preferred solution for mass flux at Mercury vs. impact velocity shows a peak at 20 km s^{-1} with and average value around 35 km s^{-1}.

Considering larger particles, Marchi et al. (2005) [56] finds a range of 15 - 80 km s^{-1} for MBAs with diameters 1 - 10^4 cm with an average value of 42 km s^{-1}. Le Feuvre & Wieczorek (2008, 2011)'s analysis of cratering in the inner Solar System found similar results as Marchi et al. (2005) - that is, a range of approximately 15 - 80 km s^{-1} [21] and an average impact velocity of 42.5 km s^{-1} [20].

A distinction in these investigations should be mentioned. Borin et al. (2009, 2016) [2, 1], Cintala (1992) [4], and Pokornỳ et al. (2018) [30] primarily focused on objects this work categorizes as meteoroids. These studies generally conclude that the most frequent impact velocities occur around 20 km s^{-1}. While Marchi et al. (2005) [56] does include particles as small as 1 cm, their analysis contains much larger particles which are not categorized as meteoroids, here. Le Feuvre & Wieczorek (2008, 2011) [20, 21] specifically focus on cratering events - so, impactors rather than meteoroids. Their studies show that these impactors have a

larger range of possible velocities with a higher average impact velocity of ~ 42 km s^{-1}. Thus, the distinction can be made that smaller objects, such as meteoroids, generally have lower impact velocities (~ 20 km s^{-1}) than the larger, impactor-class objects (~ 42 km s^{-1}). However, that does not lessen the meteoroids' importance as a surface process on Mercury.

1.1.3 Meteoroids' Influence on Mercury's Surface

Meteoroid impacts primarily play a role in surface alteration processes such as regolith and boulder breakup, regolith gardening, and release of volatiles which help form an exosphere. Kreslavsky et al. (2021) [60] surveyed images of the surface of Mercury to determine the frequency of boulders greater than 5 meters and found a dramatically reduced boulder population compared to the Moon: ~ 30 times less abundant than on the lunar highlands. They hypothesize that this deficiency is due to thermal stresses via Mercury's considerable diurnal temperature amplitude, micrometeoroic abrasion (they consider particles smaller than a 1 cm as micrometeoroids), and a thick regolith layer. In the summary of their paper, they state:

> Higher thermal stresses and more rapid thermal fatigue on Mercury may cause rapid disintegration of the upper decimeters of the boulder surface, and thus contribute to faster boulder obliteration. However, these factors alone cannot account for the observed difference in comparison to the Moon. A thicker regolith on Mercury is likely to disproportionally reduce boulder production rate. A higher micrometeoritic flux is likely to cause micrometeoritic abrasion to be an important factor, or even to be the dominant contributor to boulder degradation, in contrast to the Moon, where degradation is dominated by larger meteoritic impacts, and disproportionally shortens the boulder life time. We believe that the latter two factors (thicker regolith and higher micrometeorite flux) acting together are responsible for the observed paucity of boulders on Mercury in comparison to the Moon. [60]

Other studies have also inferred a thick regolith layer on Mercury [35, 61] attributing it to high meteoroid flux [5, 55]. That is, a high meteoroid flux contributes to the erosion of boulders, rocks, and pre-existing regolith leading to smaller particles which continually layers atop itself. In addition, larger impacts can excavate bedrock material and more boulders which become a part of the regolith-generation process. However, a consequence of a thick regolith layer, according to [60], is that impacts do not reach bedrock to excavate massive chunks of rock on Mercury as readily as on the Moon (also see [57] on other implications of a thick regolith layer). This system of excavation and erosion is referred to as regolith gardening [5, 10]. It

has also been shown that topographic diffusion resulting in crater degradation is more rapid on Mercury than the Moon and is possibly due to the high flux of high velocity meteoroid impacts [49].

Another significant result of meteoroid bombardment is the production of melt and vapor, and the devolatilization of the surface which contributes to the formation an exosphere around the planet [6, 62, 63]. Dominigue et al. (2014) [5] explains the importance of impact melt and vapor:

> [t]he melt produces glass within the regolith, and the vapor produces coatings or patinas on nearby regolith particles. These coatings and patinas contain many of the volatiles released during the impact, melt, and vaporization process, creating a repository for these elements within the regolith. The vapor also contributes to the formation of additional glass, the redistribution of volatiles, and a net loss of volatiles from the surface. [5]

The amount of impact vaporization due to meteoroid impacts is dependent on impact flux, impact velocity, meteoroid size, and composition. Cintala (1992) [4] found that Mercury hosts an impact rate 5.5 times that of the Moon with a 60% higher impact velocity and concluded that Mercury produces 14 times more impact melt and 20 times more vapor than the Moon per unit time. However, Borin et al. (2009) [2] found a dramatically greater impact rate and mass flux rate of 76 and 170 times, respectively, versus Cintala (1992)'s estimation (this stark difference is likely due to calibrating the meteoroid flux at Earth differently). More recently, Pokorný et al. (2021) [53] found a micrometeoroid (they consider diameters between 0.01 - 2mm) mass flux and energy flux at Mercury of 5.45 and 17.9 times, respectively, that at the Moon. As mentioned earlier, the meteoroid flux at Mercury differs between its day-side and night-side; this also influences the impact vaporization patterns. This is covered in depth by Pokorný et al. (2018) [30] and is supported by observations from the MErcury Surface, Space ENvironment, GEochemistry and Ranging (MESSENGER) spacecraft [64].

The high rate of impacts by meteorites releases neutral atoms, ions, and molecules from the planets surface. These particles become loosely bound via gravity to the planet, interact with Mercury's local space environment, or are lost to space. Neutrals, once released, can return to the surface or become ionized. Ions can be swept up by Mercury's magnetic field or lost to space due to the solar wind [5]. This ultimately results in a loss of elemental species from the

surface, although other process such as ion implantation (via solar wind) and meteorite impacts (and larger impacts), themselves, can replenish such lost material. Thus, meteoroid impacts are also an important process in altering the mineralogical and structural (melt and patinas) makeup of Mercury's surface.

1.2 Research Goal and Outlines

Because of the importance of meteoroids to Mercury, it is necessary to understand the composition of the meteoroid population. It is already understood that MBA, JFC, HTC, & OCC provide a majority of the meteoroid material that interacts with Mercury, but material originating from Mercury should also constitute some of the meteoroid population.

Much of the ejecta generated from impact-cratering events are retained by the planet and contribute to Mercury's dust environment, secondary crater population, or other surface processes. However, sufficiently high energy impacts can accelerate regolith and small boulders to velocities high enough to escape Mercury's Hill sphere, some of which may eventually come back to Mercury. It is not well understood how much of Mercury's meteoroid population originates from itself.

The goal of this research is to understand how much of Mercury's meteoroid population is composed of material originating from itself. Using scaling-relationships, impacts were simulated on Mercury's surface to obtain particle ejection velocities and the amount of mass capable of leaving the planet. Escaped particles have their orbital trajectories numerically propagated for up to 10,000 years to determine their fates, if they are capable of returning to Mercury, and if so, how much material is returned.

The rest of this thesis is as follows: The next chapter will briefly discuss cratering events and aspects of impacts that are important to this study (Chapter 2). Then, I will detail the models used to simulate impacts and propagate the orbital trajectories of escaped ejecta (Chapter 3). After that, I present the actual simulation methods (Chapter 4) and results (Chapter 5). Finally, I conclude the thesis with a discussion of the results in Chapter 6.

Chapter 2

Understanding Impacts

On the surface, impact craters appear as relatively uncomplicated geomorphological structures. Whether a basin or a microcrater, the general concept of cratering is indeed quite straightforward. Mass moving at a high velocity relative to a surface collides into it and generates a depression at the point of contact. The impactor is usually thought to be entirely annihilated while the target surface, as a whole, remains mostly unaltered – aside from the newly formed depression at the site of collision. The larger or faster the projectile, the bigger the resulting crater. The bigger the crater, the more mass that is propelled outwards into the surrounding environment. In the end, it reduces to the transfer of kinetic energy from the impactor to the target.

While this simplification is, for the most part, not wholly incorrect, it is just that: a dramatic oversimplification of a truly complex event. It ignores the complicated mechanical, chemical, and geophysical interactions that fully describe the properties of the projectile-target-ejecta system. To appreciate the many intricacies of impact cratering, please refer to H.J. Melosh's well known publication *Impact Cratering: A Geologic Process* [27]. Thankfully, detailed information about system dynamics such as the induced pressure wave, or the geochemical transformations incurred by the impact area are not required to model basic crater morphology, particle ejection velocity, or the amount of mass ejected from the impact. Experiments and detailed observations of impact cratering and its ejected material have shown that most impacts follow the same general trends of excavating material and depend only on basic properties such as target density and strength (as well as properties of the projectile itself, of course) to simulate crater ejecta.

2.1 Regolith/Surface

Regolith properties play a vital role in determining crater morphology and evolution [49, 57, 70]. When a cratering event occurs, it is categorized as either 'gravity-dominated' or 'strength-dominated' (though, recent work has shown the existence of a separate 'compaction-dominated' regime for porous materials [71]). A gravity-dominated event indicates that the excavation of the transient crater was halted by the force of gravity preventing more material from being displaced. The transient crater is the crater produced immediately by the impact, before displaced material on the crater wall and rim fall back down to partially refill the initial crater cavity. Richardson et al. (2007) provides an elegant definition: "[i]f the force of gravity g is much greater than the effective yield strength of the target material Y; that is, if it takes much more energy to loft the material out of the crater bowl than it takes to effectively break the material apart... [this is] a condition called gravity-dominated cratering" [32]. On the other hand, a strength-dominated event indicates that the excavation of the transient crater was halted because the surrounding target material was strong enough to withstand further removal of in-situ material. Similarly, Richardson describes strength-dominated cratering as: "[i]f the force of gravity g is much smaller than the effective yield strength of the target material Y; that is, if it takes much less energy to loft the material out of the crater bowl than it takes to effectively break the material apart..." [32].

It can be seen that a target's 'effective yield strength' is a defining property of the target material. However, the actual scientific definition of a target's 'strength' is not well constrained (see [19]). In the impact model used in this work, (Chapter 3), the 'strength' of a material simply needs to be a value with units of stress. Nevertheless, 'strength' is a vital property of the target material, along with target density, that governs crater formation and, subsequently, the amount of material ejected and its resulting launch speeds. In addition to actual physical properties of the target, a series of extra 'scaling' parameters, which are mostly dependent on the target material, are also required (see Table 3.3) to accurately model impacts. This is discussed in further detail in Section 3.2

This work assumes a uniform target material composed of regolith and small particles. Thus, the ejecta from simulated impacts are also entirely made up of regolith-like particles. While most impacts energetic enough to eject particles off the planet would excavate competent crustal material, this competent rock would be ejected at speeds and angles much lower than surface material directly surrounding the impact. This is due to the inverse relationship that as distance from the impact increases, ejection speeds and ejection angles decrease. More explicitly, material buried deep beneath the regolith layer, if ejected, will be pushed to further radial launch positions as it streamlines to the surface [24]. Chunks of crustal material much larger than regolith particles are indeed capable of being ejected from impacts as is evident from the existence of secondary craters and large boulders which often surround primaries, as well as the more elusive sesquinary craters [72, 73]. However, it is unlikely that fragments larger than a few meters in size would be capable of escaping Mercury, at least for the impact scales this investigation is concerned with (see Table 4.1) [74]. Therefore, a majority of the material which is launched quick enough to escape the planet will be composed of surface material such as regolith particles and small rocks. As mentioned previously, boulders larger than 5m are considerably less common on Mercury (relative to the Moon) and is partially believed to be a result of a regolith layer thick enough to reduce the excavation of large boulders and bedrock material (as discussed in section 1.1.3 [60, 57]). Thus, for our investigation of particles escaping the planet via impact, only considering small particles from Mercury's regolith layer is a valid assumption.

2.2 The Cratering Process

In general, cratering of solid materials follows the same procedure. Primarily, the contact and compression of the target material where the kinetic energy of the impactor is partially transferred into heat and a pressure wave that propagates radially out from the point of impact, often weakening and altering the chemical composition of the surrounding material. The induced shock and rarefaction waves accelerate the surrounding material (those which aren't compacted downwards or vaporized) to high velocities, often exceeding a few kilometers per second for craters greater than a few 10s of meters in diameter [27]. The initial path taken

by most ejecta is not a straight line up and out from the surface (though, recent investigations have found evidence of high-angle, high-velocity ejecta very close to the point of impact that is not captured in current impact models [68]), but rather parabola-like curves (hydrodynamic streamlines; often referred to as the Maxwell-Z model of excavation flow [24]) that follow the expanding hemispherical shocks below the surface. Once particles following these curves exit the topmost layer of the target, their paths are no longer influenced by the shock wave or impeded by surrounding material, allowing them to follow ballistic trajectories.

The velocities and trajectories that particles take heavily depend on where they exit the surface. Particles very close to the impact site will be launched at higher velocities and steeper angles, whereas those far from the impact are launched more slowly and at shallower angles. This velocity-position relationship closely follows a power-law and far from the impact site, ejection velocities decrease to zero. This implies that only the closest ejected material will have velocities high enough to escape Mercury while a majority of the launched material will remain bound to the planet and contribute to forming an ejecta blanket or secondary craters around the impact. Material launched near the crater radius, where the velocity is near zero, tend to pile up and form a small ridge, or rim, around the edge of the crater called an overturn flap. The resulting crater formed by excavation of the target site is called the transient crater.

After the formation of the transient crater, displaced material along the steep walls and rim become unstable due to gravity and will fall back down towards the center of the crater. This modification results in the crater becoming slightly wider and shallower as material refills the central pit, often forming a breccia lens above the initial impact melt [55].

Most craters are categorized as either ‘simple’ or ‘complex’ - inferred primarily by the morphology of the final crater. Simple craters are characterized by their classic circular bowl shape and have a depth $\sim$ $1/3$ to $1/5$ of its diameter. Complex craters are larger than simple craters and often have a raised peak at the center of the crater floor. This is a result of the target material rebounding after being initially compressed by the impact. Just as when one drops a rock into water, the water refills the crater and jets up from the point of impact. When sufficiently energetic impacts occur, the target is subjected to such high temperatures and pressures that the target briefly acts as a fluid before cooling and solidifying. Complex craters also have

flat floors and are much shallower, relative to their diameter, than simple craters. The transient craters formed by these larger impacts likely initially appear as larger simple craters, but greater amounts of material begin to refill the central pit resulting in flatter floors and shallower relative depths. The transition from a simple crater to a complex crater is dependent, primarily, on surface gravity, thus it is different for most bodies. On Earth, the transition occurs when the crater is around 2 km in diameter, 7 km on Mars, 12 km on Mercury, and about 15 km on the Moon. The difference in transition size for Mars versus Mercury, though they have nearly identical surface gravity, might be due to different surface or crustal strengths as well as the greater mean velocity of impacts on Mercury [28].

A third category of crater morphology exits, though it represents the largest impacts: basins. Because of their complexity and that they are well beyond the crater sizes considered here, they will not be covered. However, it should be mentioned that, compared to simple and complex craters, these massive impacts would no doubt excavate the most material and be capable of launching the greatest amount of ejecta into orbit.

The next chapter will explain how we model impacts and their ejecta.

Chapter 3

Modeling Impacts and their Ejecta

Simulating ejecta being launched off of Mercury requires some mathematical formulation to quantify the positions and velocities of material excavated by cratering events. This work makes use, primarily, of the ejecta-scaling-modelling scheme developed by Housen & Holsapple (2011) [17] to obtain particle ejection speeds (Sections 3.1.1, 3.1.2, & 3.1.3) and the amount of mass ejected (Section 3.1.5) for a single impact event into Mercury's regolith layer (Section 3.2). Then, an ejecta-plume model from Richardson et al. (2007) [32] is applied to the launched particles to give them a direction of motion (Section 3.1.4). The particles that are launched at speeds greater than Mercury's escape velocity (4.25 km/s) are eventually transferred to an N-body numerical integrator to propagate their orbital trajectories (Section 3.3).

The next few sections include derivations of some of the core relationships which form the impact dynamics model used in this study. Much of them follow the ideas and solutions derived from [14, 15, 16, 17]. For clarity, the author of this thesis did not create or contribute to any of the methods discussed in this section - he implemented them into computer simulations. The full derivations and background theory influencing the development of these impact-scaling laws is beyond the scope of this thesis – please refer to the original texts cited above for more in-depth information.

3.1 Impact Dynamics Model

The scaling relationships developed by Housen & Holsapple (2011) [17] are the primary source for the ejecta-model in this work. It seeks to quantify impact crater radius, particle ejection velocities, and amount of mass ejected based on the properties of the impactor and the target.

These properties include: the radius (a), speed (U), and bulk density (δ) of the impactor; the density (ρ), and strength (Y) of the target; and surface gravity (g).

The model starts by assuming an impact can be treated as a point-source. Consequentially, multiple characteristic dimensions need not be considered to define the scale of the impact (that is, a defining the length scale, a/U defining a time scale, and δa^3 defining a mass scale). Assuming a point source allows for these three independent dimensions (length, time, mass) to be combined into a single power-law 'coupling parameter' that fully characterizes the impactor [15]:

$$C = aU^{\mu}\delta^{\nu} \tag{3.1}$$

Holsapple (1993) describes it as

> the sole measure of the coupling of the energy and momentum of the impactor into the planetary surface. It must then determine all subsequent scaling laws for all phenomena appropriately determined by the far-field solution. This coupling parameter is determined by the two exponents μ and ν. Therefore, all scaling laws of impact processes will involve those exponents in some specific way. [16]

This point-source assumption has been shown to hold for distances as close as approximately one impactor radius away from the point of impact [16]. Thus, beyond this distance is considered 'far-field.'

At the core of developing the following scaling relationships (besides the point-source assumption) is the nondimensionalization technique of the Buckingham Pi Theorem [65]. It states that an equation with n variables consisting of k unique physical dimensions can be rewritten with $p = n - k$ dimensionless parameters (denoted π_1, π_2, ... π_p). A few relationships important to this study can now be derived.

3.1.1 Particle Ejection Speed as a Function of Position

To develop a relationship between the speed of ejected particles and distance from an impact in the gravity regime, one must assume a functional dependence on the properties of the projectile (a, U, δ) and the target (ρ, g; considering the strength-regime would use Y in place of g),

and position (x). Because of point-source scaling, the projectile properties can be written as Eq.(3.1):

$$v = f(aU^{\mu}\delta^{\nu}, \rho, g, x) \tag{3.2}$$

This function has $n = 5$ terms constructed from $k = 3$ physical dimensions (length, mass, & time). The Buckingham Pi theorem states that this system can be reconstructed with $p = 2$ nondimensional parameters. For gravity-dominated impacts, the π groups can be formed around v and g – that is, the repeating variables will be $aU^{\mu}\delta^{\nu}$, ρ and x.

The π_1 parameter can be expressed:

$$\pi_{1_v} = v\left[aU^{\mu}\delta^{\nu}\right]^a[\rho]^b[x]^c \tag{3.3}$$

Denoting the units of meters as L (for 'length'), kilograms as M (for 'mass'), and seconds as T (for 'time'), rewrite Eq. (3.3) as

$$\begin{aligned}\pi_{1_v} &= \left(\frac{L}{T}\right)\left[(L)\left(\frac{L^{\mu}}{T^{\mu}}\right)\left(\frac{M^{\nu}}{L^{3\nu}}\right)\right]^a\left[\frac{M}{L^3}\right]^b[L]^c \\ &= \left(\frac{L}{T}\right)\left[\frac{L^{1+\mu-3\nu}M^{\nu}}{T^{\mu}}\right]^a\left[\frac{M}{L^3}\right]^b[L]^c\end{aligned} \tag{3.4}$$

Next, three equations can be constructed to find expressions for the unknown exponents (a, b, c) that will nondimensionalize the parameter (i.e set units to to zero).

$$L: 0 = 1 + a(1 + \mu - 3\nu) - 3b + c \tag{3.5}$$

$$M: \quad 0 = a\nu + b \tag{3.6}$$

$$T: \quad 0 = -1 - a\nu \tag{3.7}$$

which has the solutions $a = {}^{-1}/_{\mu}$, $b = {}^{\nu}/_{\mu}$, and $c = {}^{1}/_{\mu}$. Plugging these values into Eq. (3.3) gives the first nondimensional group

$$\pi_{1_v} = \left(\frac{\rho}{\delta}\right)^{\frac{\nu}{\mu}}\frac{v}{U}\left(\frac{x}{a}\right)^{\frac{1}{\mu}} \tag{3.8}$$

The π group may be manipulated into a more convenient form, as long as it remains dimensionless [66]. So, raise Eq. (3.8) to the power μ to obtain:

$$\pi_{1_v} = \frac{x v^{\mu} \rho^{\nu}}{a U^{\mu} \delta^{\nu}} \tag{3.9}$$

The same procedure is used about g to obtain π_2:

$$\pi_{2_v} = g \left[a U^{\mu} \delta^{\nu}\right]^{a} [\rho]^{b} [x]^{c} \tag{3.10}$$

Solving its system of equations gives $a = {}^{-2}/_{\mu}$, $b = {}^{2\nu}/_{\mu}$, and $c = 1 + {}^{2}/_{\mu}$ and plugging back into Eq. (3.10) gives the second nondimensional group

$$\pi_{2_v} = \frac{x^{\frac{2}{\mu}} (gx) \rho^{\frac{2\nu}{\mu}}}{\left(a U^{\mu} \delta^{\nu}\right)^{\frac{2}{\mu}}} \tag{3.11}$$

which can be raised to the power ${}^{\mu}/_{2}$ to obtain the cleaner (and just as valid) form:

$$\pi_{2_v} = \frac{x (gx)^{\frac{\mu}{2}} \rho^{\nu}}{a U^{\mu} \delta^{\nu}} \tag{3.12}$$

Finally, the system can be expressed by the two nondimensional groups as $\pi_{1_v} = f(\pi_{2_v})$, or

$$\frac{x v^{\mu} \rho^{\nu}}{a U^{\mu} \delta^{\nu}} = f\left(\frac{x (gx)^{\frac{\mu}{2}} \rho^{\nu}}{a U^{\mu} \delta^{\nu}}\right) \tag{3.13}$$

This equation can be rearranged to get the ratio of particle launch speed to impactor speed:

$$\frac{v}{U} = \left[\frac{x}{a}\left(\frac{\rho}{\delta}\right)^{\nu}\right]^{\frac{-1}{\mu}} \hat{f}\left\{\frac{x}{a}\left(\frac{ga}{U^2}\right)^{\frac{\mu}{2+\mu}}\left(\frac{\rho}{\delta}\right)^{\frac{2\nu}{2+\mu}}\right\} \tag{3.14}$$

where $\hat{f} = f^{1/\mu}(X^{(2+\mu)/2})$; this form is directly from Eq.(4) of [17]. However, when near the impact (but still in the 'far-field' where the point-source assumption holds), gravity should not play a major role in particles' launch speeds. More explicitly, gravity would only affect particle launch speeds near the edge of the crater. As explained by [17], "the kinetic energy associated with a particle in the excavation flow is large compared to both the work done against the

gravity-induced shear strength of the target material and the change in gravitational potential energy incurred as the particle travels to the surface." Thus, the second term in Eq.(3.14) should be negligible, reducing to

$$\frac{v}{U} = C_1 \left[\frac{x}{a} \left(\frac{\rho}{\delta} \right)^{\nu} \right]^{\frac{-1}{\mu}} \tag{3.15}$$

where C_1 is a scaling constant related to material properties of the target (see Section 3.2) and can be determined from curve fitting.

Because only the fastest moving ejecta – those capable of escaping Mercury's gravity – are of interest, Eq. (3.15) could be justified as a sufficient stopping point. Provided some minimum distance from the point of impact (where material begins to be launched outwards rather than compacted downwards and the point-source assumption is valid), one can calculate a majority of the ejecta velocity profile with confidence. However, the full ejecta model should still be considered (here and in the simulation code).

As the distance from the impact approaches the crater radius, ejection velocities become small and can no longer be modeled by a power-law, but rather an asymptote that goes to zero. Thus, it follows that the ejection velocity versus position profile will depart from a power-law and become asymptotic close to the crater edge. Therefore, a relationship for crater radius and impactor properties will be derived next by following similar procedure.

3.1.2 Crater Radius in the Gravity Regime

As with particle ejection speed, the resulting impact crater radius (R) depends on the properties of the impactor and the surface. Again, working within the gravity regime and maintaining the impactor point-source assumption (Eq.(3.1)):

$$R = f(aU^{\mu}\delta^{\nu}, \rho, g) \tag{3.16}$$

This relationship can be expressed with only one π group

$$\pi_R = R \left[aU^{\mu}\delta^{\nu} \right]^a \left[\rho \right]^b \left[g \right]^c \tag{3.17}$$

and considering the variables' dimensions

$$\pi_R = (L)\left[\frac{L^{1+\mu-3\nu}M^{\nu}}{T^{\mu}}\right]^{a}\left[\frac{M}{L^3}\right]^{b}\left[\frac{L}{T^2}\right]^{c} \tag{3.18}$$

Solving for a, b, c such that $L^0M^0T^0$ produces $a = \frac{-2}{2+\mu}$, $b = \frac{2\nu}{2+\mu}$, and $c = \frac{\mu}{2+\mu}$. Because there is not another π group that can be functionally related to π_R, it must equal some constant H_1

$$\pi_R = \frac{\rho^{\frac{2\nu}{2+\mu}} g^{\frac{\mu}{2+\mu}} R}{(aU^{\mu}\delta^{\nu})^{\frac{2}{2+\mu}}} = H_1 \tag{3.19}$$

To obtain the form given by [17], Eq. (3.19) must be manipulated quite a bit:

$$\begin{aligned} R &= H_1 a^{\frac{2}{2+\mu}} \left(\tfrac{g}{U^2}\right)^{\frac{-\mu}{2+\mu}} \left(\tfrac{\rho}{\delta}\right)^{\frac{-2\nu}{2+\mu}} \\ \Rightarrow \frac{R}{a} &= H_1 \left(\tfrac{ga}{U^2}\right)^{\frac{-\mu}{2+\mu}} \left(\tfrac{\rho}{\delta}\right)^{\frac{-2\nu}{2+\mu}} \end{aligned} \tag{3.20}$$

and introducing the mass of the impactor, assuming a sphere with constant density: $m_i = \frac{4\pi a^3}{3}\delta$ implying $a \propto \left(\frac{m_i}{\delta}\right)^{1/3}$. Thus,

$$\begin{aligned} R\left(\tfrac{m_i}{\delta}\right)^{-\frac{1}{3}} &= H_1 \left(\tfrac{ga}{U^2}\right)^{\frac{-\mu}{2+\mu}} \left(\tfrac{\rho}{\delta}\right)^{\frac{-2\nu}{2+\mu}} \\ \Rightarrow R &= H_1 \left(\tfrac{ga}{U^2}\right)^{\frac{-\mu}{2+\mu}} \left(\rho^{\frac{-2\nu}{2+\mu}}\right)\left(\rho^{\frac{1}{3}}\rho^{-\frac{1}{3}}\right)\left(\delta^{\frac{2\nu}{2+\mu}}\right)\delta^{-\frac{1}{3}} m^{\frac{1}{3}} \\ &= H_1 \left(\tfrac{ga}{U^2}\right)^{\frac{-\mu}{2+\mu}} \left(\tfrac{\rho}{\delta}\right)^{\frac{2+\mu-6\nu}{3(2+\mu)}} \left(\tfrac{m}{\rho}\right)^{\frac{1}{3}} \end{aligned} \tag{3.21}$$

Finally, moving the mass term to the left produces the matching form for crater radius in the gravity regime as [17]:

$$R\left(\frac{\rho}{m_i}\right)^{\frac{1}{3}} = H_1 \left(\frac{\rho}{\delta}\right)^{\frac{2+\mu-6\nu}{3(2+\mu)}} \left[\frac{ga}{U^2}\right]^{\frac{-\mu}{2+\mu}} \tag{3.22}$$

3.1.3 Final Particle Ejection Speed Model for Impacts Normal to Surface

Now, with a relationship for ejecta speed $v = f(aU^{\mu}\delta^{\nu}, \rho, g, x)$ and one for crater radius $R = f(aU^{\mu}\delta^{\nu}, \rho, g)$ which share a common set of parameters, they can be related to one another in the form $v = f(R)$. With careful observation, one will notice a glaring similarity between the $\hat{f}$ term in Eq. (3.14) and Eq. (3.20):

$$\frac{x}{a}\left(\frac{ga}{U^2}\right)^{\frac{\mu}{2+\mu}}\left(\frac{\rho}{\delta}\right)^{\frac{2\nu}{2+\mu}} = H_1\frac{x}{R} \tag{3.23}$$

Thus, the ejecta launch speeds can be rewritten as a function of crater radius

$$\frac{v}{U} = \left[\frac{x}{a}\left(\frac{\rho}{\delta}\right)^{\nu}\right]^{\frac{-1}{\mu}} f\left(\frac{x}{R}\right) \tag{3.24}$$

Note that because x and R have the same dimensions of length, we can reduce the $\hat{f}() \rightarrow f()$ [66]. With this new relationship, a transition between the power-law governing most of the particle ejection speeds and an asymptote bringing ejection speeds to zero nearing the crater edge, can be developed. More generally, a boundary conditions for the whole function can be derived.

Directly surrounding the impact, all material is assumed to be compacted downwards, but at some distance $x = n_1 a$ away from the impactor, material will begin to be ejected outwards. Far away from the impact, near the crater rim $x = n_2 R$, the ejection speed of material will go to zero. The scaling terms n_1 and n_2 are constants; a value of 1.2 is typically used for n_1 and the value of n_2 will differ between target materials and whether the impact is in the strength or gravity regime, but is typically between 1 - 1.5. Housen & Holsapple (2011) adopt $\left(1 - \frac{x}{n_2 R}\right)^p$ for $f(x/R)$ in Eq. (3.24) [17]. This gives the final formulation for particle ejection speeds due to a normal incidence impact as a function of ejection position as given in [17] and which is used in this work:

$$\frac{v}{U} = \left[\frac{x}{a}\left(\frac{\rho}{\delta}\right)^{\nu}\right]^{-1/\mu}\left(1 - \frac{x}{n_2 R}\right)^p, \quad n_1 a \leq x \leq n_2 R \tag{3.25}$$

Like the other constants, p is determined by fitting these relationships to empirical data. This relationship can be used to describe ejecta in both the strength and gravity regimes. Here, the equation was derived assuming the gravity regime, but ultimately the effect of strength, Y, meets the same fate as gravity, g. That is, that close to the impact the amount of energy transferred to particles is assumed to make surface strength a negligible factor. Though, the

effects of surface strength become important as ejection velocities go to zero; this is captured by the n_2 term.

3.1.4 Particle Ejection Angles, Directions, and Adjustments to Velocity for Oblique Impacts

So far, the impact dynamics model has only considered scalar values. Particle ejection speeds can now be calculated, but nothing has been said about ejection angles or directions. Richardson et al. (2007) [32] developed a first-order model for ejecta plume behavior based on the Deep Impact cratering event on Comet Tempel 1. As with previous sections, the information presented here is from [32]. The author of this thesis did not derive nor contribute to the development of the model. All the information in this subsection is credited to Richardson et al. (2007) and their references. Much of their model originates from [14, 15, 16]. However, to model the evolution of the plume, they must consider the angle of incidence of the impactor, and the subsequent ejection angles of the ejecta.

In considering a normal incidence impact, they assume a monotonically decreasing ejection angle with increasing distance from the point of impact. They adopt the function

$$\psi_n(x) = \psi_0 - \psi_d \left(\frac{x}{R} \right) \tag{3.26}$$

where ψ_n is the particle ejection angle, ψ_0 is the "starting angle," ψ_d is the "total drop" angle, x is distance from the impact, and R is the crater radius. The ψ_0 and ψ_d values were determined from least-squares fits by [3] and have values $52.4^\circ \pm 6.1^\circ$ and $18.4^\circ \pm 8.2^\circ$ respectively.

Oblique impacts are, unsurprisingly, slightly more complicated to model. According to Richardson et al. (2007),

> an oblique impact will affect the cratering event in four basic ways: the transient crater volume and size will be smaller; particle ejections angles will be lowered on the down-range side of the ejecta plume; particle ejection velocities will be higher on the down-range side of the ejecta plume; and the ejecta plume mass-loading will be shifted toward the down-range side. [32]

Because the impact is no longer one-dimensional, both the vertical and horizontal components of the projectile's kinetic energy and momentum must be accounted for. Experiments have shown that the vertical component of the impactor's kinetic energy and momentum are what

govern the resulting crater size. The horizontal components, however, are what influences the mass excavation flow – shifting ejection directions down-range, increasing this down-range ejection velocity and lowering ejection angle [32]. The more oblique an impact, the more exaggerated these characteristics.

A one-dimensional, normal incidence impact requires that ejecta move in at least two spatial dimensions (up and out). Assuming the target surface is uniform and the impactor is spherical, the two dimensional ejecta can simply be rotated around the vertical axis to produce a three-dimensional ejecta plume. That is to say that calculating the ejecta launch angles for a normal incidence impact only requires knowledge of two dimensions and the third dimension can be assumed to be symmetric. An oblique impact, however, will require knowledge of all three dimensions because it is not symmetric about the vertical axis. Eq. (3.26) is already a function of two dimensions – radial distance (x) and the vertical dimension which is contained in the calculation of crater radius R. Richardson et al. (2007) introduces the oblique-impact particle launch angle equation:

$$\psi_f(x,\theta) = \psi_n - \left[30^\circ \left(\cos\phi\right)\left(\frac{1-\cos\theta}{2}\right)\left(1-\frac{x}{R}\right)^2\right] \tag{3.27}$$

where ϕ is the angle of incidence of the impact (90° is defined to be normal to the target surface) and θ is the azimuthal angle of the ejected particle with reference to the incoming horizontal direction of the impactor (i.e. 180° is directly down-range and 0° is opposite the impactor's horizontal direction of travel). With the inclusion of the particle azimuth θ, this equation accounts for all the required three spatial dimensions.

The change in particle ejection velocity due to an oblique impact as compared to normal should directly be related to how the ejection angle changed (assuming this change in ejection angle is due to altering the horizontal component of the particle's velocity). Therefore, Richardson et al. (2007) uses:

$$v_f(x,\theta) = \left[\left(v\sin\psi_n\right)^2 + \left(\frac{v\sin\psi_n}{\tan\psi_f}\right)^2\right]^{1/2} \tag{3.28}$$

where v is the normal particle ejection speed from Eq. (3.25) [32].

3.1.5 Amount of Mass Ejected

With the information and methods that have been discussed, developing a relationship for the amount of mass ejected at a velocity greater than v becomes straightforward. As before, assume that mass ejected is a function of the impactor, surface, and distance from the impact site.

$$M_{ej} = f(aU^{\mu}\delta^{\nu}, \rho, x) \tag{3.29}$$

Inclusion of the variable x is what relates the amount of mass ejected to ejection velocities. As one moves away from the point of impact, the amount of mass ejected from within x will monotonically increase, but at each position x, the mass ejected from that spot will have some specific velocity value. There is clearly an inverse relationship between the two – as more mass is ejected (i.e. x increases), the velocity of the ejecta decreases. Thus, if the relationship depends on x, it can only provide information about the mass ejected from inside that distance, or the amount of mass ejected at speeds greater than the velocity at that point. The relationship with v also captures the effects (or lack thereof) of gravity, g, and strength, Y, for their respective regimes.

As before, using the dimensional analysis of the Buckingham Pi theorem:

$$\begin{aligned} \pi_M &= M_{ej}\left[aU^{\mu}\delta^{\nu}\right]^a\left[\rho\right]^b\left[x\right]^c \\ &= (M)\left[\frac{L^{1+\mu-3\nu}M^{\nu}}{T^{\mu}}\right]^a\left[\frac{M}{L^3}\right]^b\left[L\right]^c \end{aligned} \tag{3.30}$$

Because the coupling parameter is the only term with units of time, it must disappear, so $a = 0$. Then, $b = -1$ and $c = -3$. Only a single π term is allowed for this system. Thus, π_M must equal some constant k:

$$\begin{aligned} \pi_M &= \frac{M_{ej}}{\rho x^3} = k \\ \Rightarrow M_{ej} &= k\rho x^3 \end{aligned} \tag{3.31}$$

As one approaches the point of impact, or rather the region of compaction around the impact $x = n_1 a$, the amount of mass ejected goes to zero. Considering this limit, as well as normalizing to the mass of the impactor $m = \frac{4}{3}\pi a^3 \delta$, gives the model for the amount of mass ejected:

$$\begin{aligned} \frac{M_{ej}}{m} &= \frac{3k\rho}{4\pi\delta}\left(\frac{1}{a^3}\left[x^3 - (n_1 a)^3\right]\right) \\ &= \frac{3k}{4\pi}\frac{\rho}{\delta}\left[\left(\frac{x}{a}\right)^3 - n_1^3\right] \end{aligned} \tag{3.32}$$

As per usual, the value of the constant k is determined from empirical data and differs based on the target material, though is generally in the range of 0.2 - 0.5 [17].

3.2 Target Properties

No mission set to investigate Mercury has returned rock or regolith samples, and unlike the Moon and Mars, there are no known meteorites on Earth that definitively originated from the Hermean surface. This means that nearly all of Mercury's relevant surface properties must be assumed, primarily, from data collected by the Mariner 10 and MESSENGER spacecrafts. Such data has allowed for extensive investigations into the planet's composition and history.

The surface of Mercury is often compared to that of the Moon [75, 29]. Both bodies display an abundant cratering record and the presence of distinct geologic regions: older, more heavily cratered highlands and the younger, smoother maria (Moon) and plains (Mercury) which indicates both were once geologically active [25]. Neither body has an atmosphere, which makes their surfaces more susceptible to impacts, space weathering, and regolith production [5, 34, 31]. Based on their locations in the inner Solar System and current crater populations, it is believed that both the Moon and Mercury's impactor flux are comparable and originate from the same sources (that is, MBA, JFC, HTC, & OCC) [7, 8, 21, 26, 30].

As shown in the previous section, the impact model requires 'scaling' terms which are mostly dependent on the target's material properties. These terms must be obtained experimentally or via curve fitting. Experiments to determine these values have been conducted on a wide range of materials such as sand, glass micro-spheres, weak basalt and various other sand mixtures [3, 17], but not on lunar regolith samples. Fortunately, much of the Moon's geology and

Table 3.1. Scaling laws used to simulate gravity-dominated impacts and the resulting ejection velocities

Parameter	Equation	Units
Strength/Gravity regime transition	$\rho U^2 \left[\frac{ga}{U^2}\left(\frac{\delta}{\rho}\right)^{1/3}\right]^{\frac{2}{2+\mu}}$	Pa
Crater volume (V_g)	$H_1 \frac{m}{\rho}\left(\frac{ga}{U^2}\right)^{-\frac{3\mu}{2+\mu}}\left(\frac{\rho}{\delta}\right)^{\frac{\mu}{2+\mu}}$	km^3
Crater radius (R_g)	$H_1 \left(\frac{\rho}{\delta}\right)^{\frac{2+\mu-6\nu}{3(2+\mu)}}\left(\frac{ga}{U^2}\right)^{-\frac{\mu}{2+\mu}}\left(\frac{m}{\rho}\right)^{1/3}$	km
Ejecta velocity (v_g)	$C_1 U\left[\frac{x}{a}\left(\frac{\rho}{\delta}\right)^{\nu}\right]^{-1/\mu}\left(1-\frac{x}{R_g n_{2g}}\right)^{p}$	km s^{-1}
Ejection angle for normal-incidence impact (ψ_{ng})	$\psi_0 - \psi_d\left(\frac{x}{R_g}\right)$	radians
Ejection angle for oblique impact (ψ_{fg})	$\psi_{ng} - \left[30^\circ \cos(\phi)\left(\frac{1-\cos(\theta)}{2}\right)\left(1-\frac{x}{R_g}\right)^2\right]$	radians
Ejection velocity for an oblique impact	$\left[(v_g \sin(\psi_{ng}))^2 + \left(\frac{v_g \sin(\psi_{ng})}{\tan(\psi_{fg})}\right)^2\right]^{1/2}$	km s^{-1}
Mass ejected quicker than v (M)	$\frac{3k}{4\pi}\frac{\rho}{\delta}\left[\left(\frac{x}{a}\right)^3 - n_1^3\right] m$	kg

Note. — Equations for regime transition, V_g, R_g, v_g, and M come from [17]. The equation for M can be used for both gravity and strength dominated impacts. Equations for ψ_{ng}, ψ_{fg}, and ejection velocity for an oblique impact come from [32]. Values for the target properties ρ and g and scaling constants μ, H_1, C_1, $n1$, n_{2g}, ν, p, and k can be found in Table 3.3. Values for the impactor properties, a, δ, m, U and ϕ can be found in Table 4.1. $\psi_0 = 52.5^\circ$ and $\psi_d = 18.5^\circ$ as given by [32]. The variable x represents the radial distance away from the point of impact. The variable θ is the azimuthal angle from 0° to 359° around the impact site with 180° in the downrange direction.

Table 3.2. Scaling laws used to simulate strength-dominated impacts and the resulting ejection velocities

Parameter	Equation	Units
Crater volume (V_s)	$H_2 \frac{m}{\rho} \left(\frac{Y}{U^2 \rho} \right)^{-\frac{3\mu}{2}}$	km^3
Crater radius (R_s)	$H_2 \left(\frac{\rho}{\delta} \right)^{\frac{1-3\nu}{3}} \left(\frac{Y}{U^2 \rho} \right)^{-\frac{\mu}{2}} \left(\frac{m}{\rho} \right)^{1/3}$	km
Ejecta velocity (v_s)	$C_1 U \left[\frac{x}{a} \left(\frac{\rho}{\delta} \right)^{\nu} \right]^{-\frac{1}{\mu}} \left(1 - \frac{x}{R_s n_{2s}} \right)^{p}$	km s^{-1}
Ejection angle for normal-incedence impact (ψ_{ns})	$\psi_0 - \psi_d \left(\frac{x}{R_s} \right)$	radians
Ejection angle for oblique impact (ψ_{fs})	$\psi_{ns} - \left[30^\circ \cos(\phi) \left(\frac{1-\cos(\theta)}{2} \right) \left(1 - \frac{x}{R_s} \right)^2 \right]$	radians
Ejection velocity for an oblique impact	$\left[(v_s \sin(\psi_{ns}))^2 + \left(\frac{v_s \sin(\psi_{ns})}{\tan(\psi_{fs})} \right)^2 \right]^{1/2}$	km s^{-1}

Note. — Equations for regime transition, V_s, R_s and v_s come from [17]. Equations for ψ_{ns}, ψ_{fs}, and ejection velocity for an oblique impact come from [32]. Values for the target properties ρ and Y and scaling constants μ, H_2, C_1, n_{2s}, ν, p, and k can be found in Table 3.3. Values for the impactor properties, a, δ, m, U and ϕ can be found in Table 4.1. $\psi_0 = 52.5^\circ$ and $\psi_d = 18.5^\circ$ as given by [32]. The variable x represents the radial distance away from the point of impact. The variable θ is the azimuthal angle from 0° to 359° around the impact site with 180° in the downrange direction.

Table 3.3. Target properties used in impact simulations

Parameter	Symbol	Value	Units
Gravity	g	3.7	m s^{-2}
Escape Velocity	v_{esc}	4.25	km s^{-1}
Strength	Y_t	4000	Pa
Surface Density	ρ_t	1500	kg m^{-3}
Scaling Constant	μ_t	0.4	-
Scaling Constant	C_1	0.55	-
Scaling Constant	k	0.3	-
Scaling Constant	H_1	0.7	-
Scaling Constant	H_2	0.4	-
Scaling Constant	n_1	1.2	-
Scaling Constant	n_{2g}	1.3	-
Scaling Constant	n_{2s}	1	-
Scaling Constant	p	0.3	-
Scaling Constant	ν	0.4	-

Note. — Gravity and escape velocity are properties of Mercury. Scaling constants, strength, and density values from impact experiments into various mixtures of sand and perlite [17, 18].

surface properties have been thoroughly investigated and are well understood [9, 10, 11, 12], making it possible to simulate lunar regolith by mixing appropriate materials to obtain similar bulk density, particle size distribution, geometry, porosity, and shear and tensile strengths (for example, the recent work by Li et al. (20221)[22]; as well as University of Central Florida's Exolith Lab). Of the currently available material-scaling data, the mixture of sand and perlite [17, 18] appear to be a good simulant of lunar regolith, and therefore is likely an acceptable simulant of Mercury regolith [75, 34, 5]. Given this, the values listed in Table 3.3 are used to simulate the surface properties of Mercury in all of our simulations.

3.3 Orbit Propagation Model

Immediately after ejection from the surface, particles briefly follow ballistic trajectories and are then transferred to an orbit propagation code (N-body code) to numerically integrate their orbital trajectories. Particle motion is considered to be ballistic for as long as the ground beneath them can be approximated to be flat. Quantitatively, this work uses multiples of crater formation time (typically 5x) for ballistic propagation before being handed off to the N-body code. The N-body dynamics code implements a 4th order Runge-Kutta integration scheme to calculate particle trajectories. It considers the gravity of 10 major bodies – all 8 planets, the Sun, and Earth's moon – and includes perturbative effects of solar radiation pressure (SRP) and Poynting-Robertson drag (PRD). Particle-particle interactions (gravitational, electrostatic, frictional forces and collisions) and particle self-gravity are not included in the model.

The orbital motion of a particle, which is here denoted using index i, is given by

$$\ddot{\mathbf{r}}_i = \mathbf{a}_i^g + \mathbf{a}_i^{pert} \tag{3.33}$$

where $\mathbf{r}_i$ is the heliocentric position vector, $\mathbf{a}_i^g$ is the gravitational acceleration, and $\mathbf{a}_i^{pert}$ is the non-gravitational acceleration.

For $\mathbf{a}_i^g$, the particle i is considered to be influenced by the bodies mentioned above, which are defined using index j, and written as

$$\mathbf{a}_i^g = -\sum_{j=1}^{j_{max}} GM_j \frac{\mathbf{r}_i - \mathbf{r}_j}{|\mathbf{r}_i - \mathbf{r}_j|^3} \tag{3.34}$$

where G is the gravitational constant, and M_j is the mass of body j. In our model, $j_{max} = 10$. On the other hand, $\mathbf{a}_i^{pert}$ is given as [45]

$$\mathbf{a}_i^{pert} = \frac{Q_{pr} L A_i}{m_i c} \left[\left(1 - \frac{\dot{r}_i}{c} \right) \hat{\mathbf{S}} - \frac{\dot{\mathbf{r}}_\mathbf{i}}{c} \right] \tag{3.35}$$

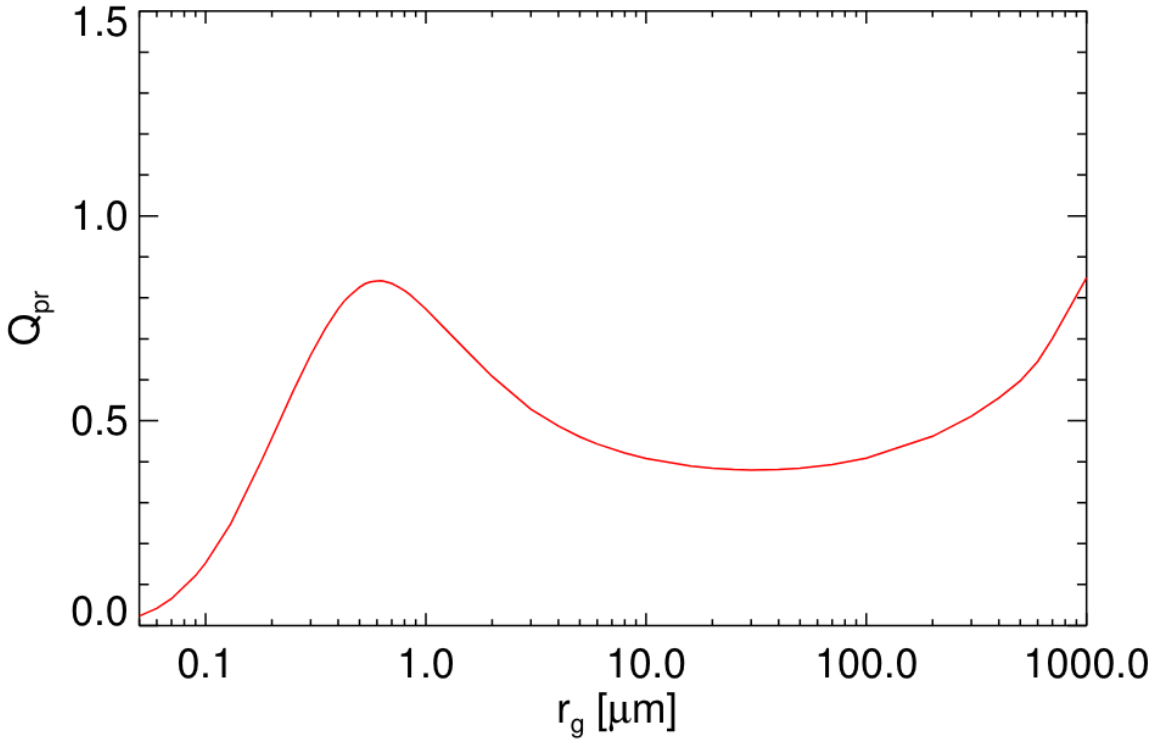

Figure 3.1 Figure 3 from Liu & Schmidt (2018) [23] showing the Mie theory calculations of radiation pressure efficiency, Q_{pr} for different particle sizes. Grains are considered to be silicate. Liu & Schmidt, A&A, 609, A57, 2018, reproduced with permission ©ESO.

where m_i is the particle mass, L is the energy flux density of the radiation field (i.e. irradiance from the Sun), $\hat{\mathbf{S}}$ is the unit radial vector from the Sun (outward positive), A_i is the cross-sectional area of the particle, c is the speed of light, Q_{pr} is the radiation pressure efficiency of the particle (via the Mie theory), and $\dot{r}_i$ is the radial component of the velocity vector (i.e., $\dot{r}_i = \dot{\mathbf{r}}_\mathbf{i} \cdot \hat{\mathbf{S}}$). The radial term is SRP, and the velocity dependent term is PRD. For particles of radius 10 µm and 100 µm, Q_{pr} = 0.42 is used. Particles with radius of 50 µm, 500 µm, and 1000 µm use Q_{pr} = 0.38, 0.60, 0.85, respectively. These values are based on Figure 3 of Liu & Schmidt's (2018) [23] calculations of the radiation pressure efficiency dependence on the size of silicate particles (Fig. 3.1). For reference, a value of zero means SRP and PRD are not active - only gravity influences particle dynamics; and the unity value indicates a totally absorbing particle and is widely used in the literature [36, 45].

The Runge-Kutta 4th-order integrator is used to solve Equation (3.33), with a time step, h, of 432 s which is obtained by dividing the number of seconds in a day by 200 ($0.005 \cdot 86400$

s). We choose this value because of its balance of accuracy and efficiency. We compared simulation results using this 432 s time step against smaller time steps such as 86 s and 43 s. The 432 s time step produced trivial differences in particle trajectories compared to the smaller time steps. Even when making multiple close approaches to the Sun, particles can remain on stable orbits and not decay due to the choice of time-step. The quasi-total energy of a test particle under $\mathbf{a}_i^g$ without $\mathbf{a}_i^{pert}$ (Eq. (1.29) in [46]) has been tested and found to be constant with negligible fluctuation. It should be noted that the Runge-Kutta integration method accumulates error on the order of h^4 [40, 41]. For the integration times and time step this projects considers, the accumulated error does not greatly influence the trajectories of the particles or massive bodies. However, if one wished to propagate trajectories for greater time-scales, such as millions of years, another integration method should be considered for better computational efficiency and reduced accumulated error.

The next chapter will describe the simulations and how they are set up.

Chapter 4

The Simulations

The following simulations implement the previously described impact and orbital dynamics models (Chapter 3). Both models were written in C++. This chapter will briefly describe the flow of the codes and how they work.

4.1 Code Validation

The impact code is validated by recreating some of the figures from Housen & Holsapple (2011) [17]. Table 2 of their paper consolidates experiments focused on measuring ejecta properties which are then used to determine scaling constants for each of the tested target materials. The resulting scaling constants for these materials are listed in Table 3 of their paper [17]. To ensure that the impact simulation code generates data accurate to the implemented scaling models, the scaling constants they present are used to recreate their Figures 13 (Fig. 4.1), 14 (Fig. 4.2) and 16 (Fig. 4.3). All of the recreations match the original figures very well.

The orbital dynamics (N-body) code has been previously validated in the publication by Jackson et al. (2022) [67].

4.2 Impact-Event Setup

Combinations of impactor radius (10 m, 50 m, 100 m, 500 m, 1000 m), impact angle (30, 45, 60, 90 degrees), and location on Mercury's surface (latitude and longitude) are employed to simulate impacts. An impact speed of 42 km s^{-1} (average speed of Mercury impactors found by [56, 20]) and an impactor density of 2500 kg m^{-3} are used for all simulations. Test particles

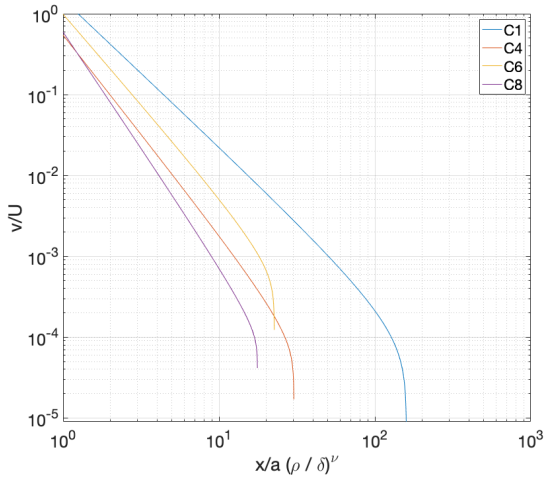

(a) Recreation

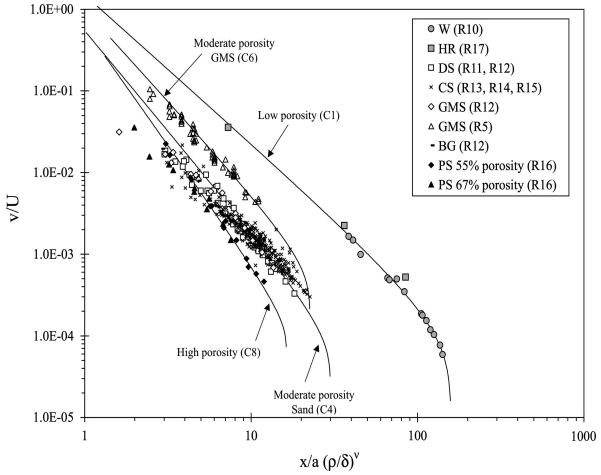

(b) Figure 13[1] from [17]

Figure 4.1 These plots effectively show ejection speed versus radial launch position in terms of impactor properties (See Eq.(3.24)). The closer the ejection position is to the site of impact, the greater the ejection speed. However, as the distance approaches the crater edge, the power-law profile begins to break down as the effects of strength or gravity begin to inhibit ejecta production and ejection speed goes to zero. The original figure (b) fits the scaling model to experimental data from the following targets: W = water, HR = hard rock, DS = dense sand, CS = coarse sand, GMS = glass micro-spheres, BG = basalt gravel, PS = Perlite/sand mixture. [1]Reprinted from Icarus, 211, Housen, K. R., & Holsapple, K. A., Ejecta from Impact Craters, 856-875, Copyright (2011), with permission from Elsevier.

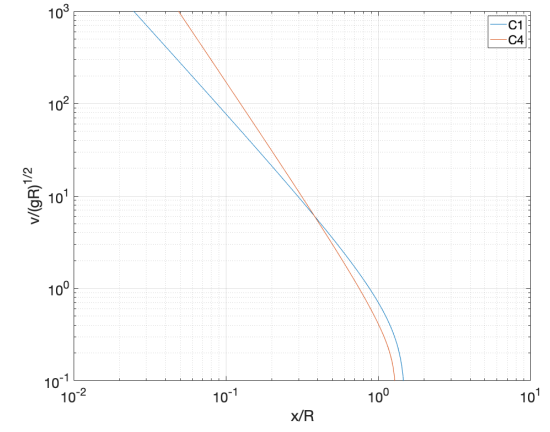

(a) Recreation

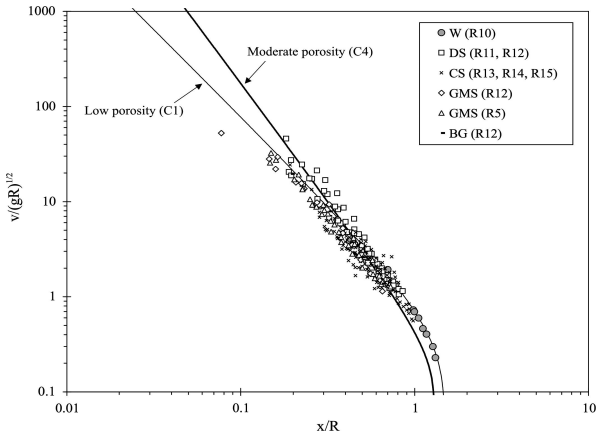

(b) Figure 14[1] from [17]

Figure 4.2 Particle ejection speed versus radial launch position in terms of crater radius for gravity-dominated impacts. [1]Reprinted from Icarus, 211, Housen, K. R., & Holsapple, K. A., Ejecta from Impact Craters, 856-875, Copyright (2011), with permission from Elsevier.

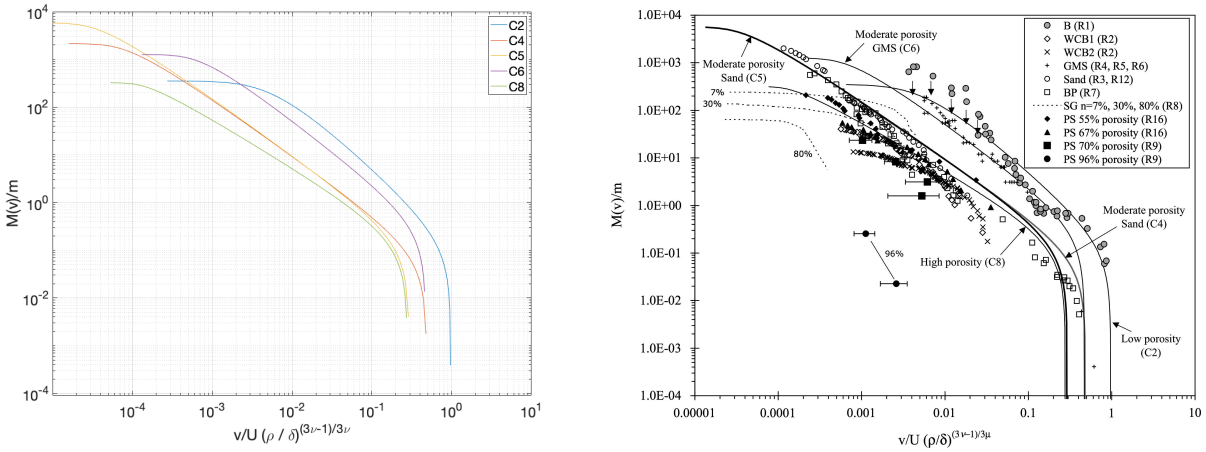

(a) Recreation

(b) Figure 16[1] from [17]

Figure 4.3 These plots show the amount of mass ejected at a speed greater than v in terms of impactor properties. Both ends of the curves deviate from the primary power-law profile due to effects of strength or gravity. Beyond the vertical asymptotes of curves, the point-source scaling breaks down. The leftmost point each curve gives the total amount of mass ejected from that impact. [1]Reprinted from Icarus, 211, Housen, K. R., & Holsapple, K. A., Ejecta from Impact Craters, 856-875, Copyright (2011), with permission from Elsevier.

are assumed to be spherically symmetric with a uniform mass density of 1500 kg m^{-3}. Particles with radii of 10 µm, 100 µm, 500 µm, and 1000 µm are considered. Figure 4.4 displays a schematic of the impact setup and important impact properties. These impact properties are also listed in Table 4.1. All combinations of impactor properties considered are capable of launching particles off Mercury and into interplanetary trajectories (see Fig. 4.5).

These impactor parameters, along with target material properties listed in Table 3.3, are used to determine whether the impact is gravity-dominated or strength-dominated which then allows for the calculation of the transient and final crater sizes. Knowing crater size then permits the calculation of particle ejection speeds as a function of distance from the impact point (see Tables 3.1 & 3.2).

At this point, the number of test particles per impact simulation should be defined; keeping in mind that the primary constraint is the amount of time it takes to propagate their orbital trajectories (and to a lesser degree, data storage of particle states at each time-step, dT). The time it takes to calculate particle ejection speeds using the scaling relationships is trivial, however all test particles must have their trajectories propagated with the N-body code, which is not trivial. The decided number of particles per impact case is 432 (coincidentally, this is the same as the

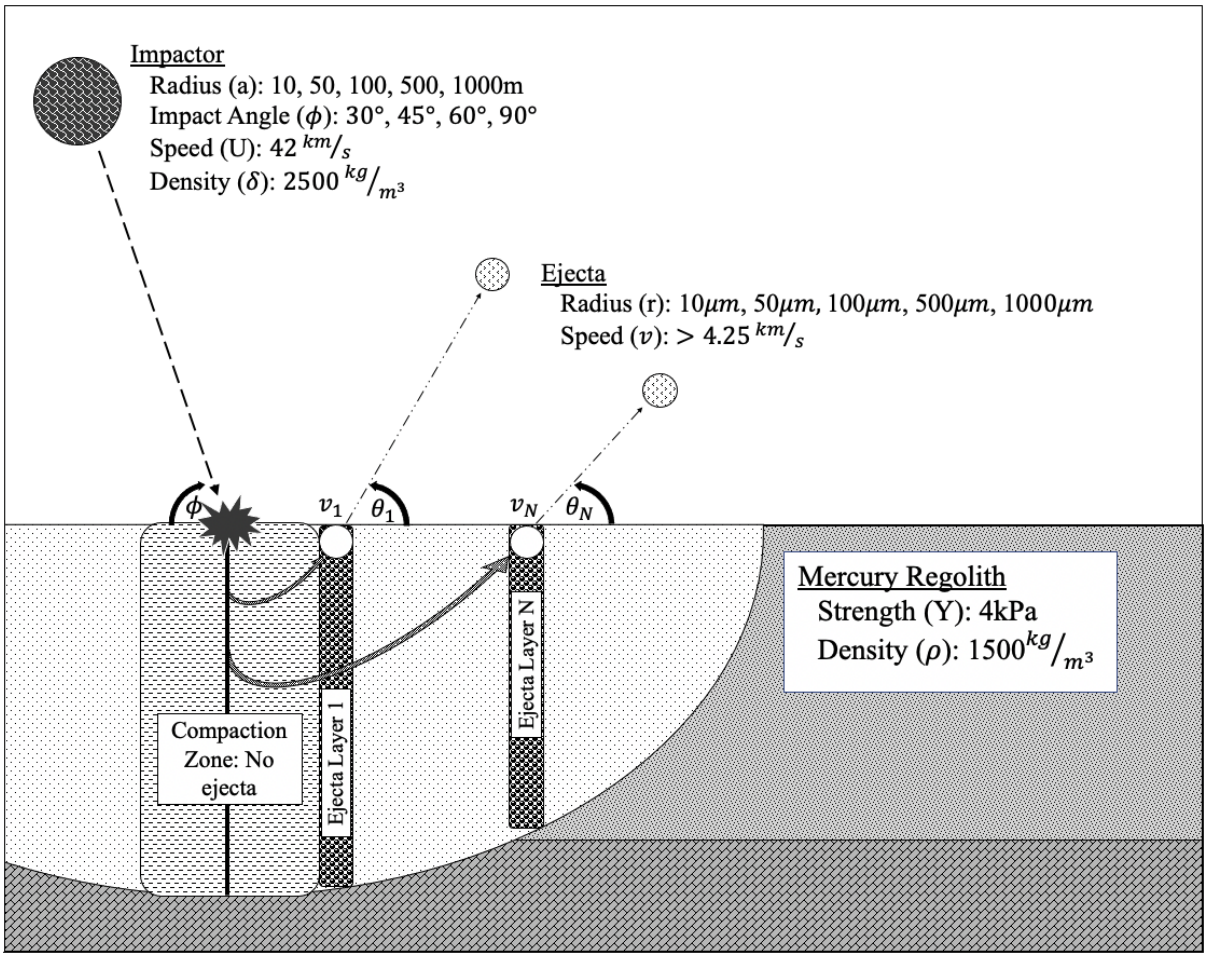

Figure 4.4 Schematic of impact simulation. N = 12 ejecta layers are rotated (not depicted) around the impact point with particles ejected every 10 degrees. This gives 432 particles per individual impact scenario. No material is ejected from the surface within the 'compaction zone.' Particles from this region, however, are pushed out and follow streamlines [24] to be ejected from the surface at greater distances from the impact.

time step value dT of the N-body code). The next few paragraphs will explain how this value was determined.

The scaling relationship for calculating particle ejection speeds takes x, the radial distance from the impact point, as an input. Because this analysis only considers particles ejected faster than Mercury's escape velocity (4.25 km s^{-1}), one can rearrange the scaling relationship to calculate the x where this occurs. This gives an outer bound for x. The inner bound for x is also known because it is assumed (to uphold the point source scaling model - see Chapter 3) that all material within $n_1 = 1.2$ times the impactor radius is compacted downwards - producing no ejecta. With an upper and lower bound for x, this range can be discretized into ejecta 'layers'

Table 4.1. Impactor properties used in impact simulations

Parameter	Symbol	Value	Units
Radius	a_i	10, 50, 100, 500, 1000	m
Density	δ_i	2500	kg m^{-3}
Mass	m_i	$\frac{4}{3}\pi\delta_i a_i^3$	kg
Impact Speed	U	42	km s^{-1}
Impact Angle	ϕ	30, 45, 60, 90	Degrees
Latitude of Impact	λ	-45, 0, 45	Degrees
Longitude of Impact	Φ	-90, 0, 90, 180	Degrees

Note. — Impactors are assumed to be spherical with uniform density. We use a single impact speed of 42 km s^{-1} [20]. An impact angle of 90° is normal to the surface.

($Radial_{mesh}$ in *Input* of Fig. 4.6). At this point, the total amount of mass that will escape the planet can be estimated using Eq. (3.32). Because this equation specifically gives the amount of mass ejected *moving at a speed greater than* v, using the point x where ejection speed is equal to the escape velocity will produce the total amount of mass capable of escaping Mercury. This scalar value considers the total amount of mass ejected in all directions, whereas our particle ejection analysis thus far has only been in two dimensions.

To create a three-dimensional plume, recall that the ejected particles will be duplicated and rotated around the point of impact. Ejecting particles once every 10^o of rotation ($Angular_{mesh}$ in *Input* of Fig. 4.6) would produce 36 particles per radial ejecta layer. Discretizing the range of x into 12 radial layers gives 12 layers $\times$ 36 $\frac{\text{particles}}{\text{layer}} = 432$ total particles for a single impact's three-dimensional ejecta plume; all of which are capable of escaping Mercury.

In addition, the benefit of having 12 discrete radial ejecta layers is that such layers can be separated from each other without a loss of continuity. That is, the layers can be further grouped into 3 categories: 'fast' (the first 4 ejecta layers closest to the impact), 'medium' (the middle 4 ejecta layers), and 'slow' (the outer 4 ejecta layers) moving ejecta. Each category has an output file generated with the state vectors of 144 particles. This file is later used as input for the N-body code. The purpose of further separating the particles from a single impact in this

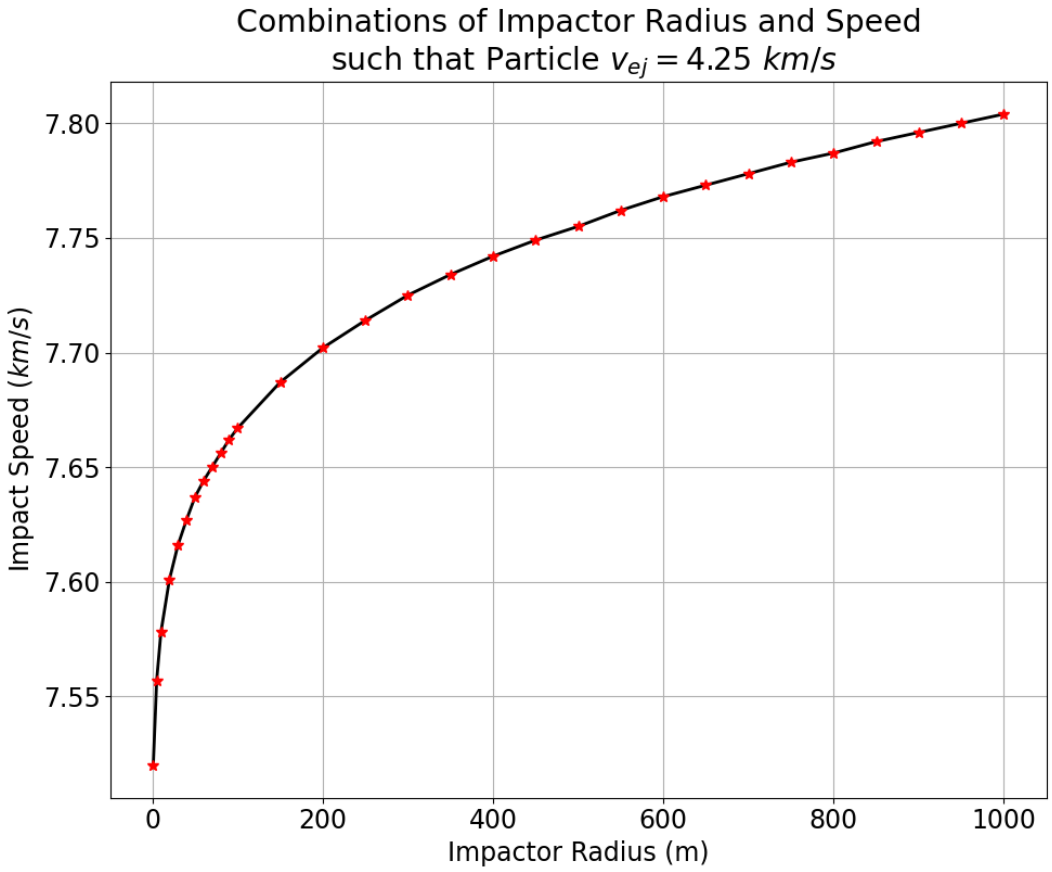

Figure 4.5 Minimum combination of impactor speed and size for the target properties in Table 3.3 that will eject particles at a speed equal to Mercury's escape velocity. Combinations below the curve will produce ejecta that remains gravitationally bound to Mercury. Combinations above the curve will begin to produce ejecta that is capable of escaping Mercury's gravity. The further above the curve, the more ejecta will escape. Naturally, one would expect that this relationship would follow a $1/x$ trend: from conservation of energy (and momentum), if the size of the impactor increases, the speed required for it to eject a particle at some constant value would decrease. This is true if the launch position of the particle also remains constant. However, as explained before, the closest point to the site of impact where material can first be ejected is a function of impactor size: $x = n_1 a = 1.2a$. Thus, as impactor size increases, the amount of energy (and, therefore, speed) needed by the impactor to eject the particle located at $x = 1.2a$ is greater than for smaller impactor radii.

way is that, instead of propagating the orbital trajectories of all 432 particles in a single N-body simulation, 3 distinct N-body simulations (per impact) can be run in parallel. This ultimately reduces the amount of time it takes to run the simulations and obtain results.

However, before the particles' state vectors can be output and transferred to the N-body code, they must first reach some altitude at which it can be justified to use orbital dynamics to model their motion. Immediately after ejection from the surface, particle motion is ballistic. Ballistic motion can be easily calculated once the particles' speeds and directions are defined.

All impact cases simulate the ballistic motion of particles for five times the gravity or strength-dominated crater formation time. There is no rigorous reason for this choice of time other than that a few multiples of crater formation time should allow for particles to travel $\sim$ 100s of km above the surface. Figure 4.7 visualizes the ballistic motion and plume of ejecta produced by an oblique impact. After this initial period of ballistic motion is the point at which the state vectors are output in a form that the N-body code will take as input.

Figure 4.6 depicts a high-level flowchart of the full simulation procedure.

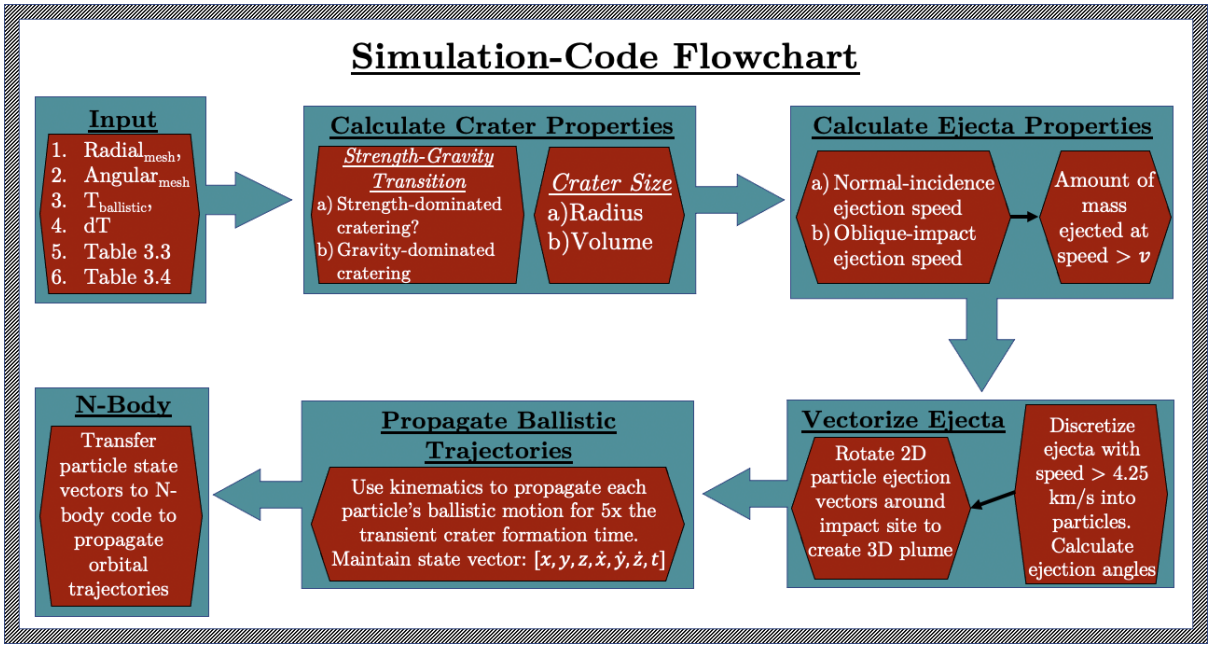

Figure 4.6 Impact Code flowchart

4.3 N-Body Code

The particle state vector files are the primary input into the N-body code. However, the code also requires a planetary ephemeris file that contains each (Sun, Mercury, Venus, Earth, Moon, Mars, Jupiter, Saturn, Uranus & Neptune) body's standard gravitational parameter, barycentric position and velocity, and time. For each massive body, every time step simply calculates the acceleration felt on it due to the gravity of all the other massive bodies. For the particles, each time step calculates the acceleration felt on it by all the massive bodies as well as the accelerations due to solar radiation pressure and Poynting-Robertson drag (See Section 3.3).

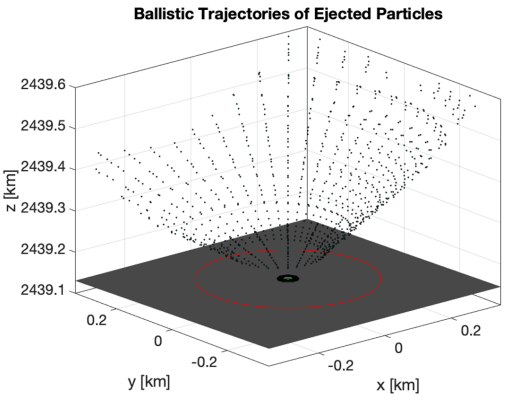

(a) Close-up view of impact.

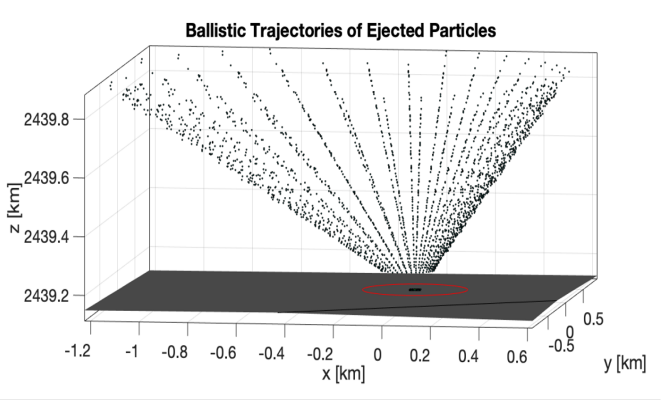

(b) Side view of impact.

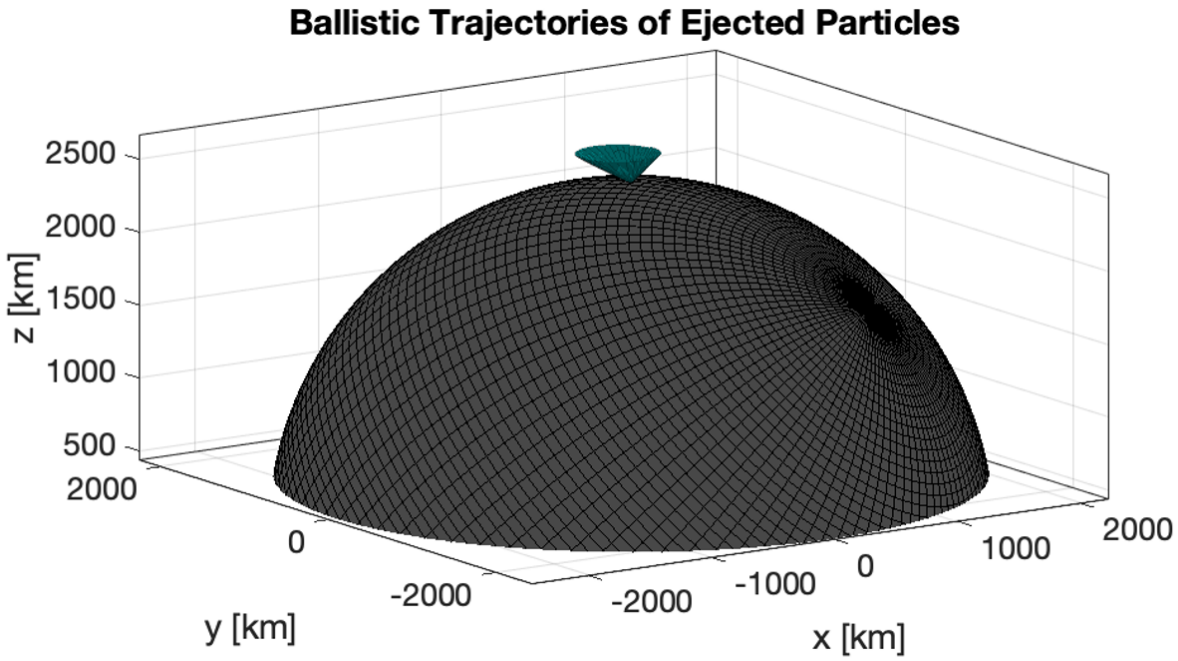

(c) Zoomed-out view of full ejecta plume visualized as a surface instead of individual points.

Figure 4.7 Ejecta from an oblique, gravity-dominated impact with paramters: $a_i = 10$m, $\phi = 30^o$, impacting at 45^oS, 90^oE on Mercury's surface with $-x$ being the downrange direction. The red circle in (a) and (b) is the resulting crater with radius = 0.215 km. The green circle at the center of the crater is the size of the impactor. The dark ring surrounding the impactor are the initial positions of the 12 ejecta layers. The fastest downrange-moving ejecta, relative to Mercury, is ~ 39.8 km s^{-1}. The average ejection speed is 13.55 km s^{-1}. The crater formation time is 4.89 seconds, so the ejecta is ballistically propagated for 24.45 seconds before being transferred to the orbital dynamics code (see Fig.4.8).

Particles are assumed to not interact with any other particles in any way. The code considers a barycentric reference frame. All simulations use a single starting epoch for our simulations: 1 January, 2026 – just after the BepiColombo mission's planned orbital insertion around Mercury.

To monitor the motion of the particles, the code outputs their state vectors as well as their distances relative to the Sun and each planet four times per Earth year. This rate of data output was chosen because doing so every timestep (432 sec) requires an unreasonable amount of data storage capability. Doing so four times per year is still frequent enough to reconstruct continuous trajectories, but with a significantly lower data storage requirement. The code can also output the Hamiltonian of each particle considering all the massive bodies (see Eq. 1.29 of [46]).

The critical piece of information that this project is interested in is whether the particles get 'intercepted' by Mercury, the Sun, or any of the other major bodies considered in the simulation. This project adopts two definitions of 'intercepted': one for planetary bodies and one for the Sun. A particle that gets intercepted by a planetary body is defined as: crossing from outside to inside the planetary body's Hill sphere. The definition used for the Sun is: approaching within 10 solar radii of the Sun. A body's Hill sphere is the boundary layer surrounding the body where its own gravitational acceleration matches that of a more massive, external body - in this case, the Sun. The radius of a body's Hill sphere can be approximated by

$$r_H \approx a_p \left(1 - e_p\right) \sqrt[3]{\frac{m_p}{3M_s}} \tag{4.1}$$

where a_p and e_p are the semi-major axis and eccentricity, respectively, of the smaller planetary body around the Sun; m_p is the mass of the smaller planetary body; and M_s is the mass of the Sun. For the Moon, the more massive external body is the Earth rather than the Sun. So, while Eq.(4.1) is still valid, the semi-major axis and eccentricity are relative to the Earth and M_s would be the mass of the Earth instead of the Sun. Table 4.2 lists the sizes of each massive body's Hill sphere.

At every time step, the code checks the location of each particle and if any have approached within a body's Hill sphere or close to the Sun. So, while other data is output only four times

Table 4.2. Hill sphere radii of relevant Solar System bodies.

Body	r_H [10^6 km]	r_H [AU]
Sun*	6.9570	0.0465
Mercury	0.1753	0.0012
Venus	1.0043	0.0067
Earth	1.4716	0.0098
Moon	0.5814	0.0004
Mars	0.9828	0.0066
Jupiter	50.5541	0.3379
Saturn	61.7741	0.4129
Uranus	66.7863	0.4464
Neptune	115.0390	0.7689

Note. — * The value used for the Sun is $10R_{\odot}$.

per year, the code is constantly checking to determine if a particle has been 'intercepted.' If a particle meets the criteria for being intercepted, it's state vector, particle identifier (a number between 1 - 432 which the particle is given when it is generated), and which body it was captured by is written to a file and the particle is then removed from the simulation. It is assumed that once a particle is 'intercepted,' it will remain gravitationally bound to the massive body and eventually impact the surface (at least for an airless body like Mercury). It should be noted that the code is set to *not* detect particles within the Hill sphere of Mercury for the first 5 days of propagation. This is to give particles sufficient time to exit the Hill sphere and to prevent false positive detections of particles within the Hill sphere at the beginning of the simulation. Figure 4.8 shows the propagated trajectories of a single ejecta layer (36 particles) from the same impact as depicted in Figure 4.7.

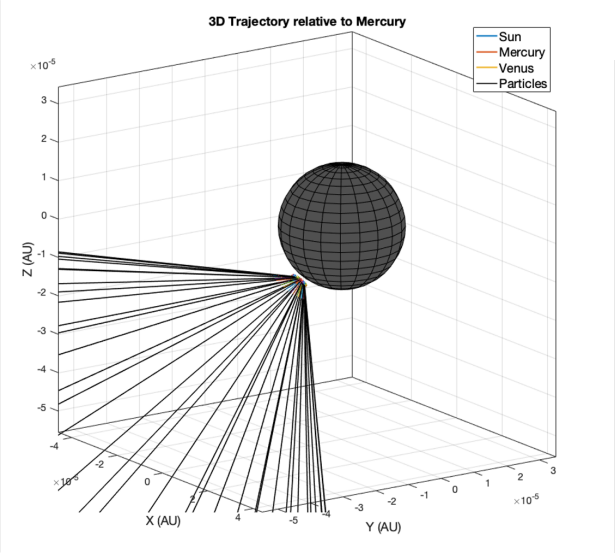

(a) Beginning of trajectory propagation. Particle vectors passed on from end of ballistic motion.

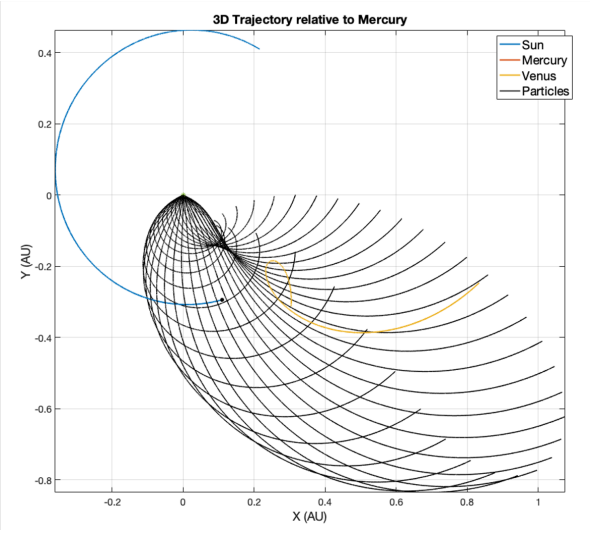

(b) Top-Down view

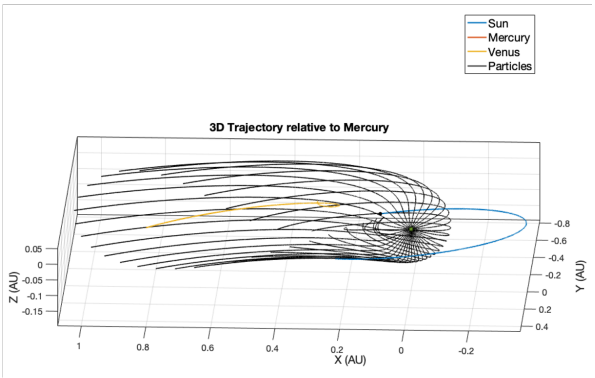

(c) Planar view from behind Mercury

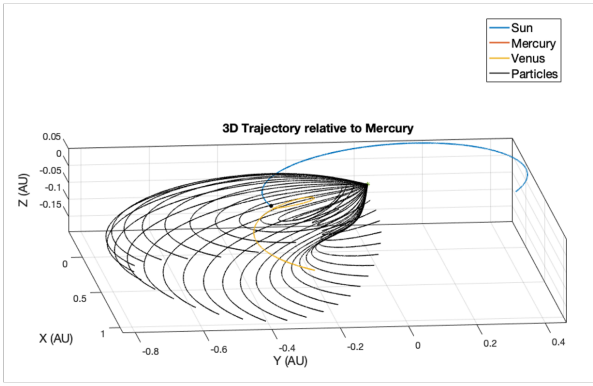

(d) Planar view from the side

Figure 4.8 Propagation of a single, medium category, ejecta layer (36, 100µm particles) from the same impact as Figure 4.7 for 36 days. These particles, in particular, had ejection speeds ranging from $11.78 - 17.94$ km s^{-1}. This reference frame is relative to Mercury.

Chapter 5

Results

This chapter will cover the results from a large number of simulations which cover different possible combinations of impactor properties (Table 4.1). The results will be displayed according to the particle radii used: 10 μm, 50 μm, 100 μm, 500 μm, & 1000 μm. The size of the particles do not affect the impact dynamics and ejection velocity, but do affect their orbital motion. This ultimately changes how many particles of a given size returns to Mercury because they will be accelerated in different amounts by solar radiation pressure and Poynting-Robertson Drag (Eq.(3.35)).

These particle sizes were chosen based on the particle size distributions of lunar regolith [11, 12, 76, 77]. Lunar regolith samples that have been analyzed are primarily composed of particles with sizes under 1000 μm (95% are finer that 1370 μm and 5% are finer that 3.3 μm)[77]. According to [11], "[t]he mean grain size of analyzed soils ranges from about 40 μm to about 800 μm and averages between 60 and 80 μm." Similarly, [76] and [77] state the average size is approximately 72 μm.

However, as explained in Chapter 1, Mercury is believed to be subjected to a greater impact rate as well as higher impact velocities. This has multiple consequences, but notably, should lead to an increased rate of regolith erosion and gardening. Thus, it is likely that the average particle grain size, as compared to the Moon, is smaller. Using remote measurements of thermal inertia, Gundlach & Blum (2013) [78] determine grain sizes of planetary regolith and estimate the mean grain radius of 48^{+115}_{-27} μm for the Moon and 22^{+46}_{-18} μm for Mercury.

The individual particle size cases obtain their results via simulating seven randomly selected impactor-combination cases (see Table 4.1 and Section 4.2) and propagating their ejecta

for 5000 years. This gives a total of 3024 particles for each size case. These cases will be presented in Sections 5.1 – 5.5. The choice of seven cases (twenty-one simulations) is simply due to computational efficiency. Only so many simulations can be run at one time and in a timely manner

Then, to simulate a more thorough and realistic case, a substantially larger simulation is run which considers all possible impactor-combinations and ejecta is propagated for a maximum of 10,000 years. This simulation does not use only one particle size, but a combination of all the individual particle sizes. The overall composition of particle radii for this large simulation are as follows: 10 μm (50%), 50 μm (40%), 100 μm (5%), 500 μm (4%), and 1000 μm (1%). This case will be presented in Section 5.6.

Though the Moon, Uranus, and Neptune were all considered capable of capturing particles in the simulations, no particles in any of the simulations ever ended up entering any of their Hill spheres. So, those three will not be included when discussing how particles dispersed to different bodies.

5.1 10 μm

Of the 3024 test particles, 2586 (85.52%) entered a massive body's Hill sphere (Figure 5.1a). Of those, only 621 (24.01%; 20.54% of total) returned to Mercury while a much larger amount, 1858 particles (71.85%; 61.44% of total), fell into the Sun. The remaining 107 captured particles (4.14%, 3.54% of total) ended up at Venus, Earth, Mars, Jupiter, or Saturn.

The average amount of time it took for particles to return to Mercury was 493.5 years. For those captured by the Sun, the average time was much longer at 2710 years. There is a grouping of about 30 - 40 particles that basically took a direct trajectory into the Sun with their average time-of-flight being approximately 0.065 years (see Fig. 5.2). The mean speed of particles re-entering Mercury's Hill Sphere was 3.42 km s^{-1} and the maximum speed was 28.62 km s^{-1}. Note that this is only the speed of the particle as it crossed into the Hill sphere. Assuming the particles will eventually be accelerated down to the surface, a mean Hill-sphere entrance speed of 3.42 km s^{-1} would translate to an impact speed of 5.43 km s^{-1}.

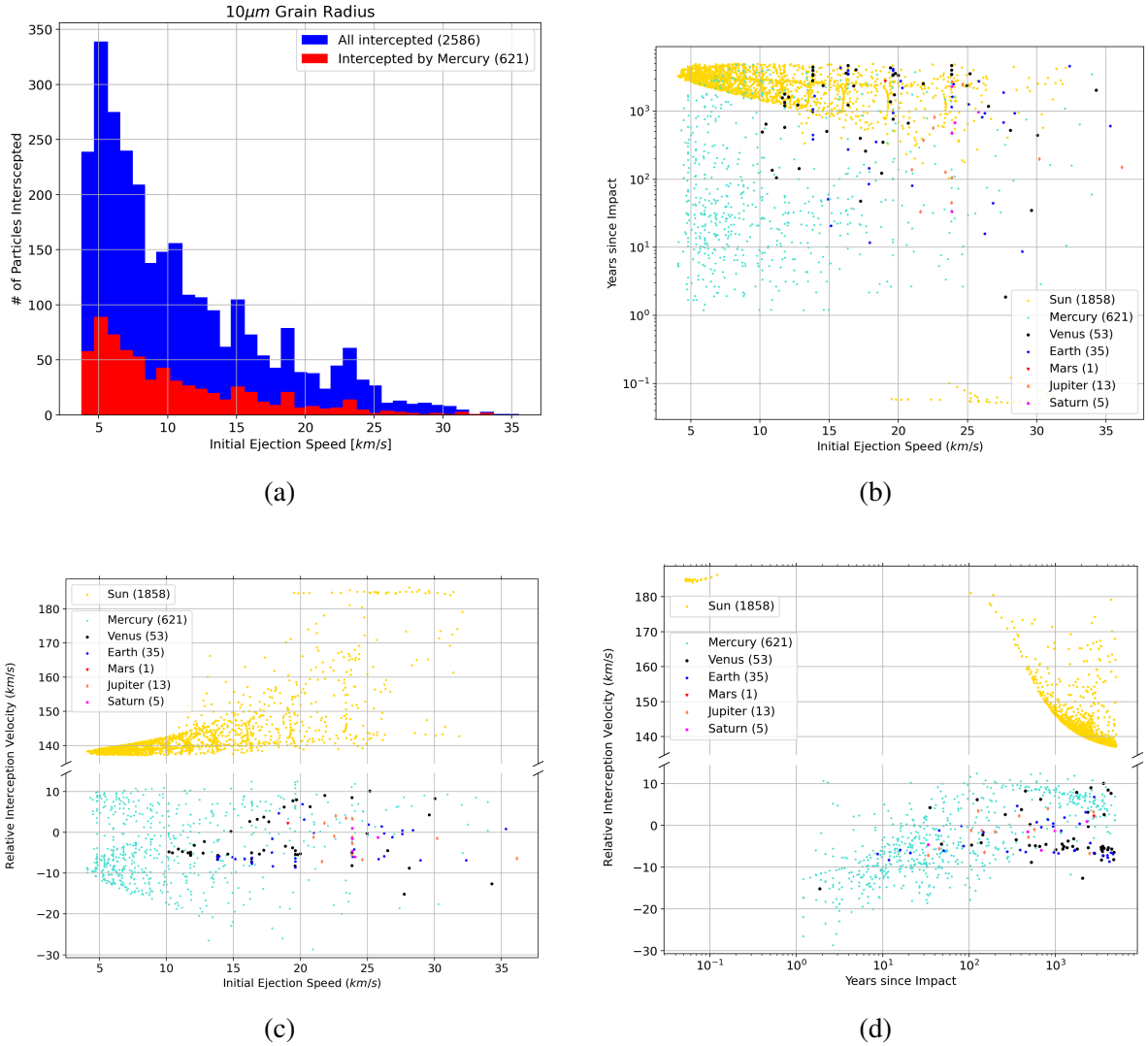

Figure 5.1 Results from 7 randomly chosen impactor property combinations which means a total of 3024 test particles. All have a grain radius of 10 µm and $Q_{pr} = 0.42$. Simulations ran for 5000 years. 2586 particles (85.52%) entered a massive body's Hill sphere, 1858 (71.85%) of which fell into the Sun (61.44% of total population). Of the 2586 that were captured, 621 (24.01%) returned to Mercury's Hill sphere. That is only 20.54% of the total. The numbers in parenthesis of the legends are the number of particles captured by that body. For plots (c) and (d), the interception speeds for each particle are relative to the body they were captured by.

5.2 50 µm

For this grain size, the percentage of particles returning to Mercury more than doubles from 20.54% (621) of the total population to 46.1% (1394). In contrast, the number of particles that were captured by the Sun dropped from 1858 to 220. This indicates that there is likely some form of a trade-off occurring between the two. Fewer particles are falling into the Sun which increases the population that could go to Mercury. In addition, the particles that were captured

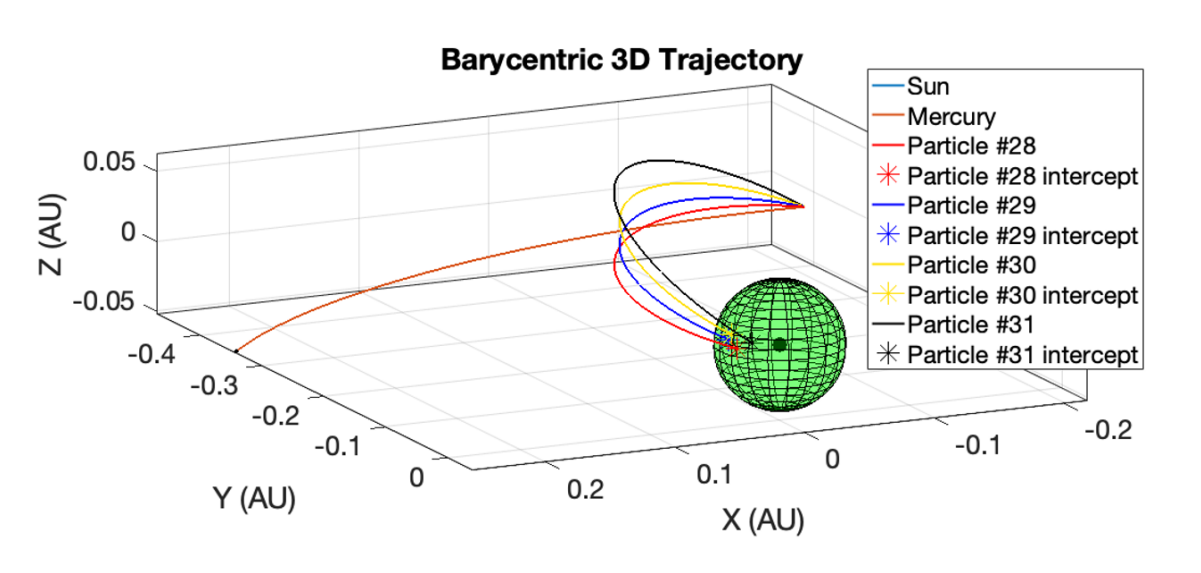

Figure 5.2 Example of 4 ejected particles taking trajectories straight from Mercury into the Sun. The green ball is Sun's effective Hill sphere (see Table 4.2). Each particle arrived at sightly different times ranging from 19.4 - 22.6 days ($\sim$ 0.06 years) after ejection. These particles had high ejection speeds of 25 - 27 km/s. Particles ejected at these speeds are less likely to return to Mercury.

by the Sun in the 10 µm case were, obviously, following trajectories very near the Sun. If these grains that were being captured by the Sun no longer are, the next easiest inner Solar System target would be Mercury itself.

The mean speed of particles returning to Mercury was 7.56 km s^{-1} which renders an average impact speed of 8.66 km s^{-1}. The maximum speed remains nearly unchanged at 28.23 km s^{-1}. The average amount of time for particles to return to Mercury was 255 years and 1110 years for the Sun.

5.3 100 µm

A trend in how many particles return to Mercury (and fall into the Sun) is now beginning to form. As with increasing the grain size from 10 µm to 50 µm resulted in more particles going to Mercury and less to the Sun, further increasing grains size to 100 µm has the same effect. 2016 (66.67%) test particles were captured with 1881 (93.3%; 62.2% of total population) returning to Mercury and only 55 (2.73%; 1.82% of total) to the Sun.

The average amount of time it took particles to return to Mercury was 191 years. This value is also beginning to follow a trend that as particle size increases, the average time particles

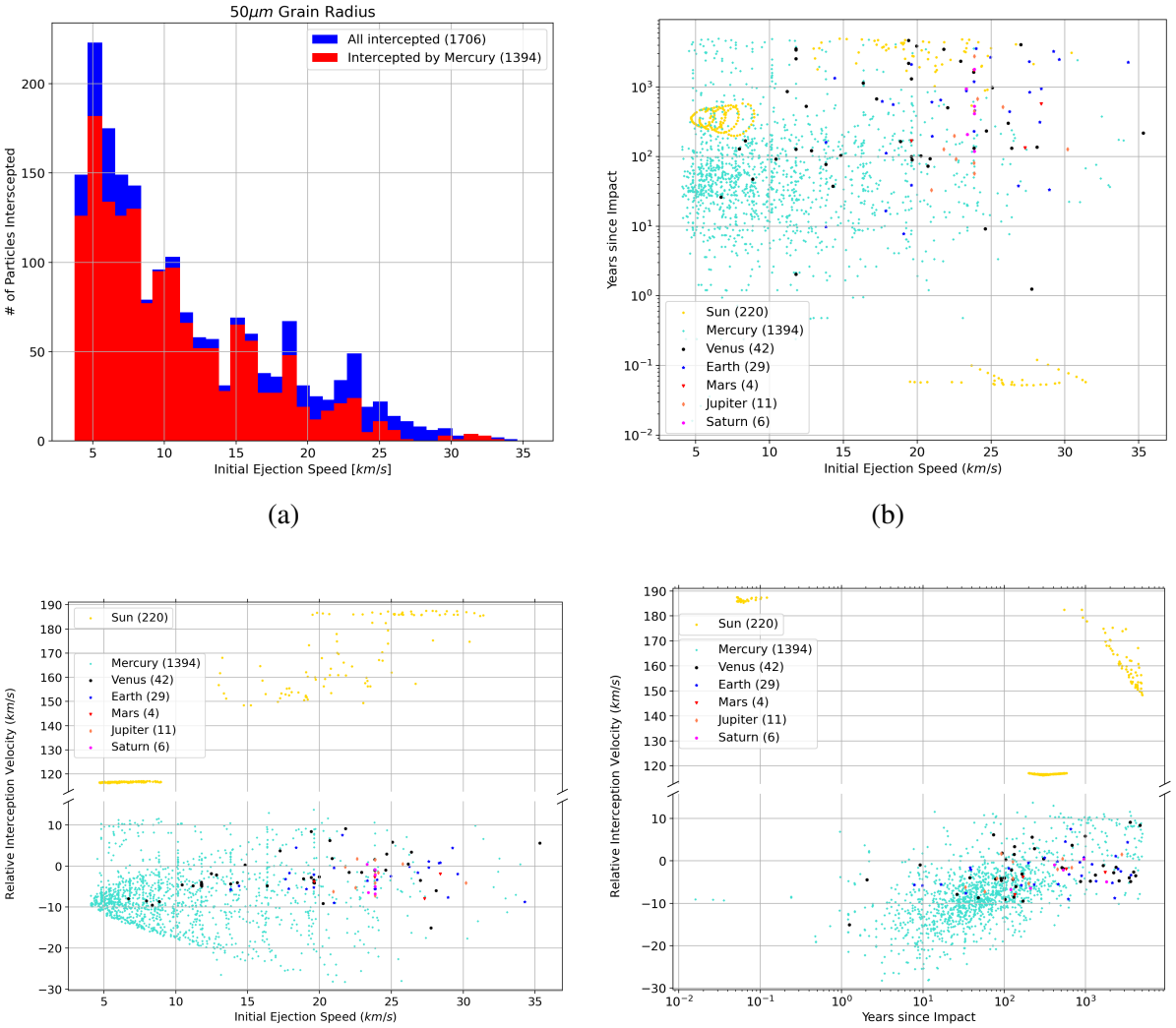

Figure 5.3 Same simulations as previously shown, though with grain radius of 50 µm and $Q_{pr} = 0.38$. These results show an increase in particles returning to Mercury as compared to the 10 µm case. 1706 particles (56.41%) entered a massive body's Hill sphere. Of those, 1394 entered Mercury's Hill sphere. That is, 81.71% of the intercepted particles and 46.1% of the total returned to Mercury.

take to return to Mercury decreases. The average capture time for particles falling into the Sun was 1214 years. The average speed of particles that crossed into Mercury's Hill sphere was 8.2 km s^{-1} and the fastest was moving at 28.54 km s^{-1}. That translates to impact speeds of 9.22 km s^{-1} and 28.85 km s^{-1}, respectively.

The trajectory of a 100 µm particle that was ejected from the impact depicted in Figures 4.7 & 4.8 and then returned to Mercury is shown in Figure 5.5. The time between impact and it re-entering Mercury's Hill sphere was 2.65 years.

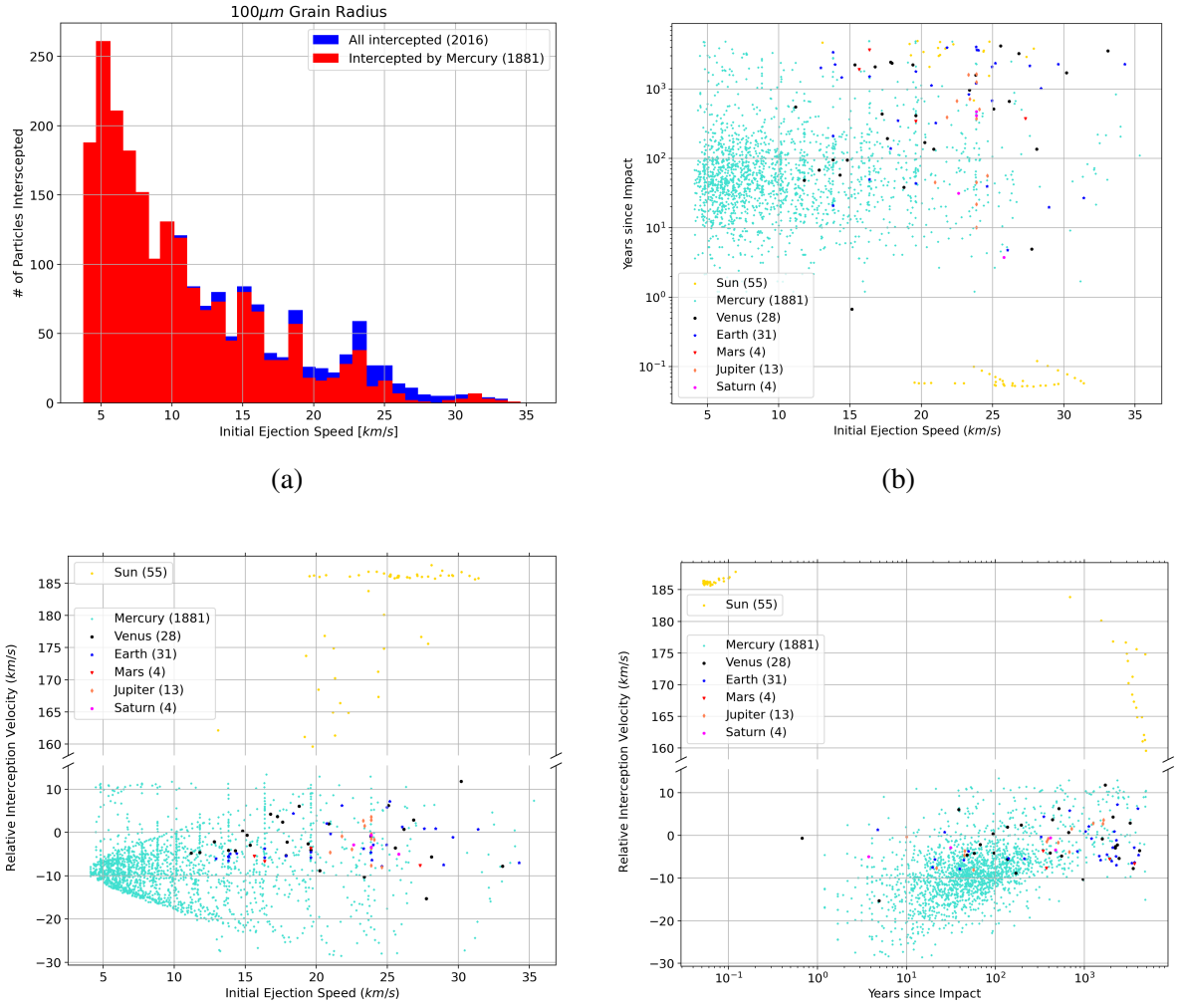

Figure 5.4 Same simulations as previously shown, though with grain radius of 100 µm and $Q_{pr} = 0.42$. 2016 particles (66.67%) entered a massive body's Hill sphere. Of those, 1881 entered Mercury's Hill sphere. That is, 93.3% of the intercepted particles and 62.2% of the total returned to Mercury.

5.4 500 µm

With the 500 µm case, the trend of increasing the total number of intercepted particles as well as the amount that goes to Mercury continues. The profiles of all the plots in Figure 5.6 are nearly identical to those of the 100 µm radius case. Of the total 3024 particles, 2569 (84.95%) were intercepted. Mercury remains the dominant sink, capturing 2437 grains (94.86%; 80.59% of total) while the amount falling into the Sun continued to decrease to only 36 particles (1.49%; 1.19% of total).

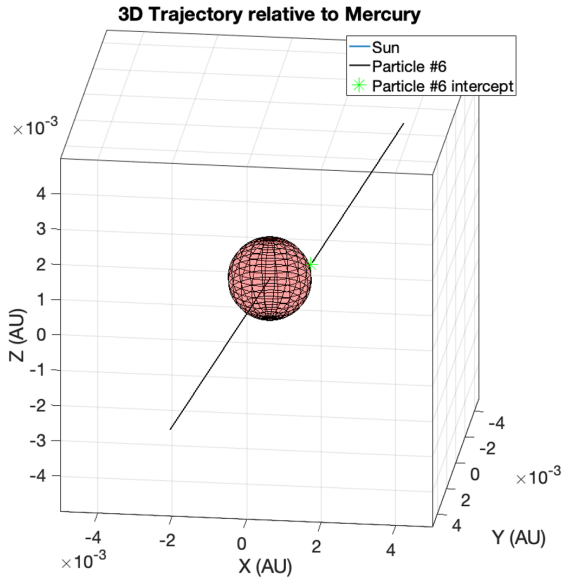

(a) Close up of a particle exiting Mercury's Hill sphere (red ball) and eventually returning.

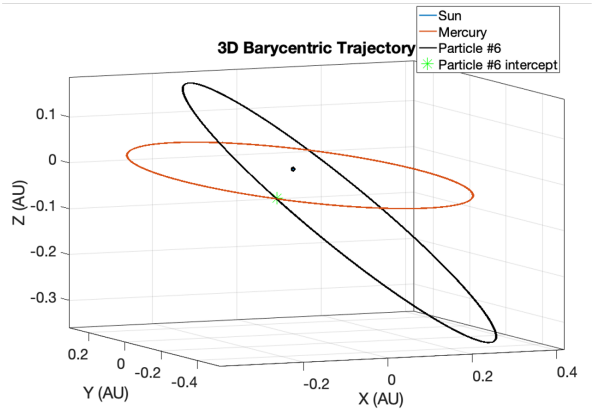

(b) Barycentric (for all intents and purposes, this is heliocentric) trajectory of the particle.

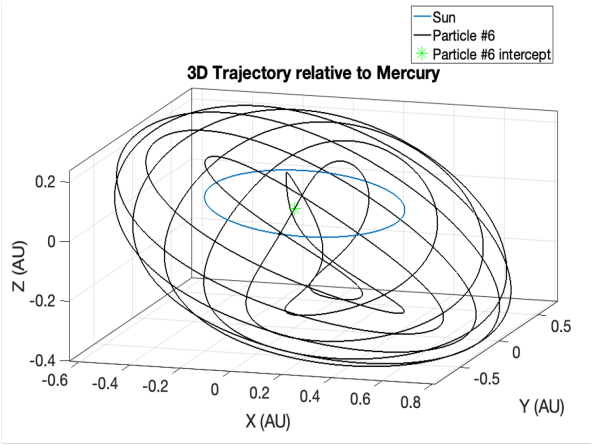

(c) Same trajectory as (b), but as seen in Mercury's reference frame.

Figure 5.5 Example trajectory of particle leaving and returning to Mercury. It was ejected by the same impact as depicted in Figures 4.7 and 4.8. Grain radius of 100 µm and $Q_{pr} = 0.42$. This particle returned to Mercury relatively quickly: 2.65 years after ejection from the impact. It was launched at a speed of 25.14 km s^{-1} and re-entered the Hill Sphere at a velocity relative to Mercury of -24.77 km s^{-1}

Particles returning to Mercury did so after an average of 139 years. Because of the minimal distribution of particles that went to the Sun, the average time it took for them to get captured was 0.064 years. The average speed at which particles entered Mercury's Hill sphere was 9.5 km s^{-1} with the maximum being 28.57 km s^{-1}. These mean impact speeds of 10.4 km s^{-1} and 28.88 km s^{-1}, respectively.

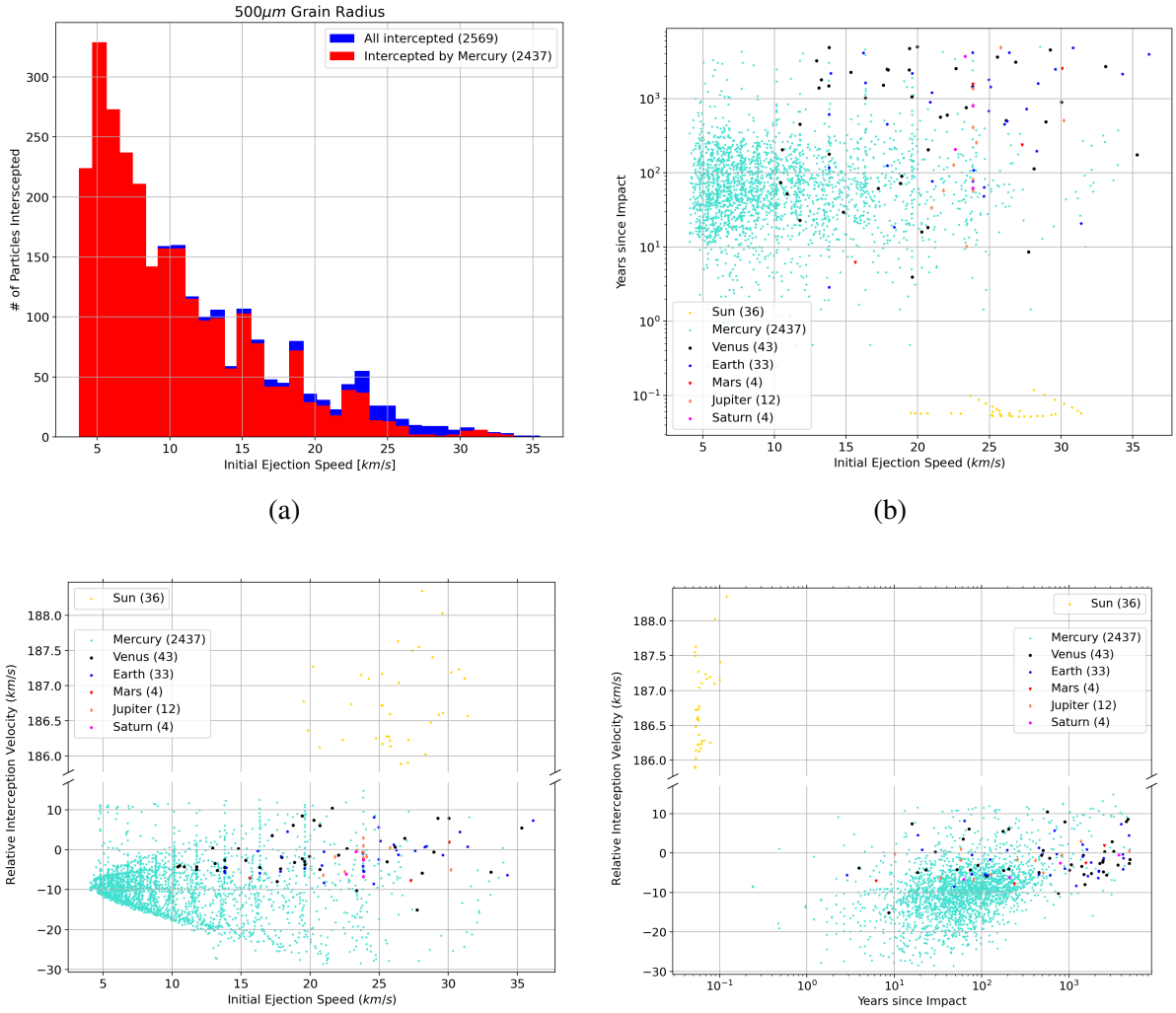

Figure 5.6 Results for grain radius of 500 µm with $Q_{pr} = 0.60$. As with the 100 µm case, nearly all of the intercepted particles were by Mercury. 2569 particles (85.95%) entered the Hill sphere of a planet or the Sun. 94.86% of them, or 2437 grains, entered Mercury's Hill sphere. That's 80.59% of the total 3024 particle population.

5.5 1000 µm

Like the previous few cases, particles with radii of 1000 µm follow the tendencies to increase the number of particles going to Mercury as well as increasing these particles' impact velocities, though at a reduced rate. The differences between the 500 µm case and this one are minimal compared to those between the 10 µm to 50 µm, 50 µm to 100 µm, and 100 µm to 500 µm cases.

An overwhelming majority of the particles that were captured were by Mercury. Of the 3024 test particles, 2616 (86.51%) were captured. Of those captured, 2482 (94.88%; 82.08% of

total) returned to Mercury, 36 (1.38%; 1.19% of total) were sucked up by the Sun, and the rest of the 98 (3.75%; 3.24% of total) captured particles were dispersed between the other planets.

Particles returning to Mercury took an average of 153 years. Like the previous case, the number of particles going to the Sun is small, so might not be statistically significant. Nevertheless, the average time for particles falling into the Sun remained as 0.064 years. The average and maximum interception speeds were also nearly identical to the previous case: 9.55 km s^{-1} and 28.56 km s^{-1}.

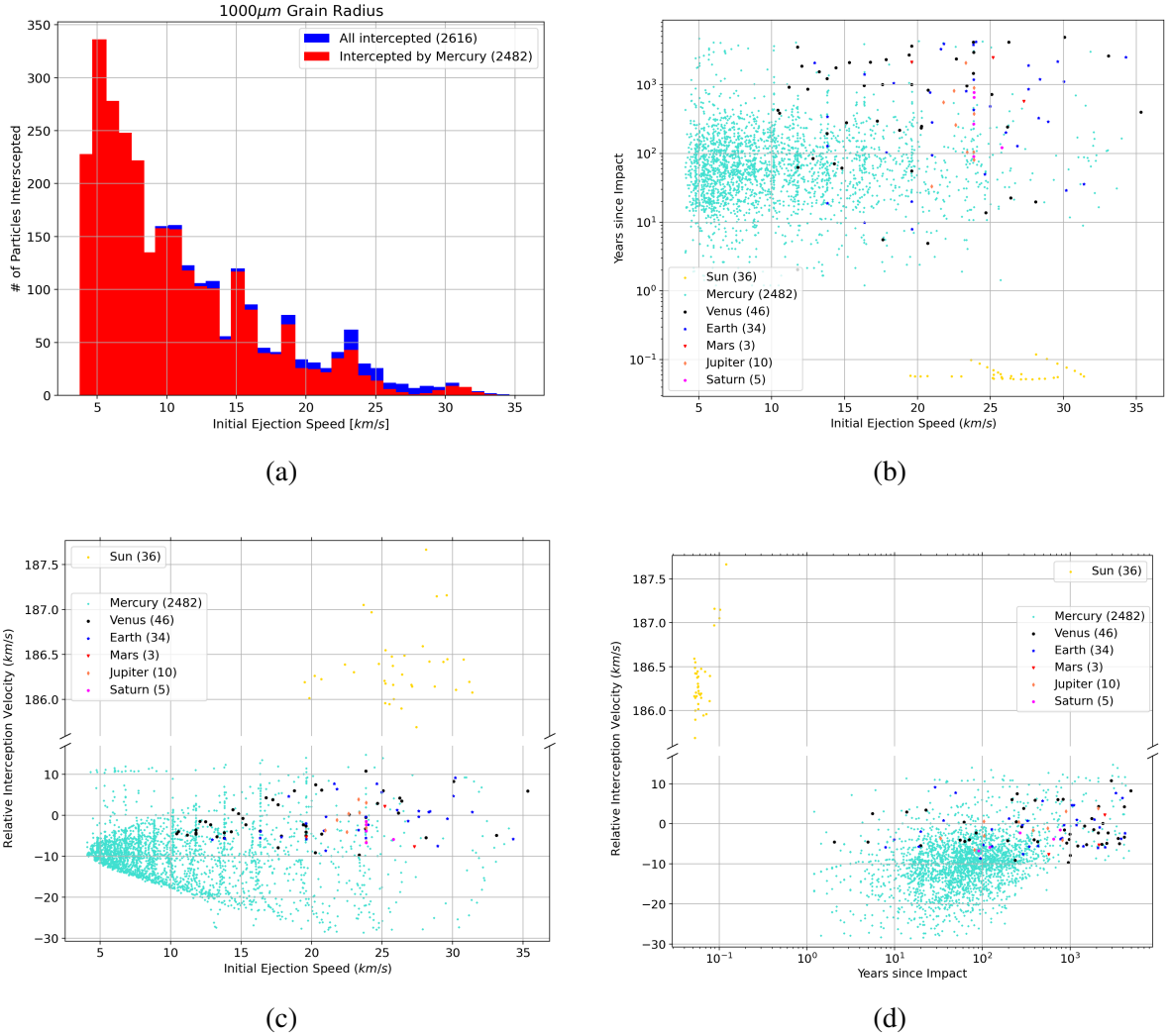

Figure 5.7 5000 year simulations of grains with radius of 1000 µm and $Q_{pr} = 0.85$. 2616 particles (86.51%) entered a massive body's Hill sphere. Of those, 2482 entered Mercury's Hill sphere. That is, 94.88% of the intercepted particles and 82.08% of the total returned to Mercury.

Out of all of these size cases, the particles that were not captured mostly remain within the inner Solar System and have just not been intercepted yet. A small portion of particles

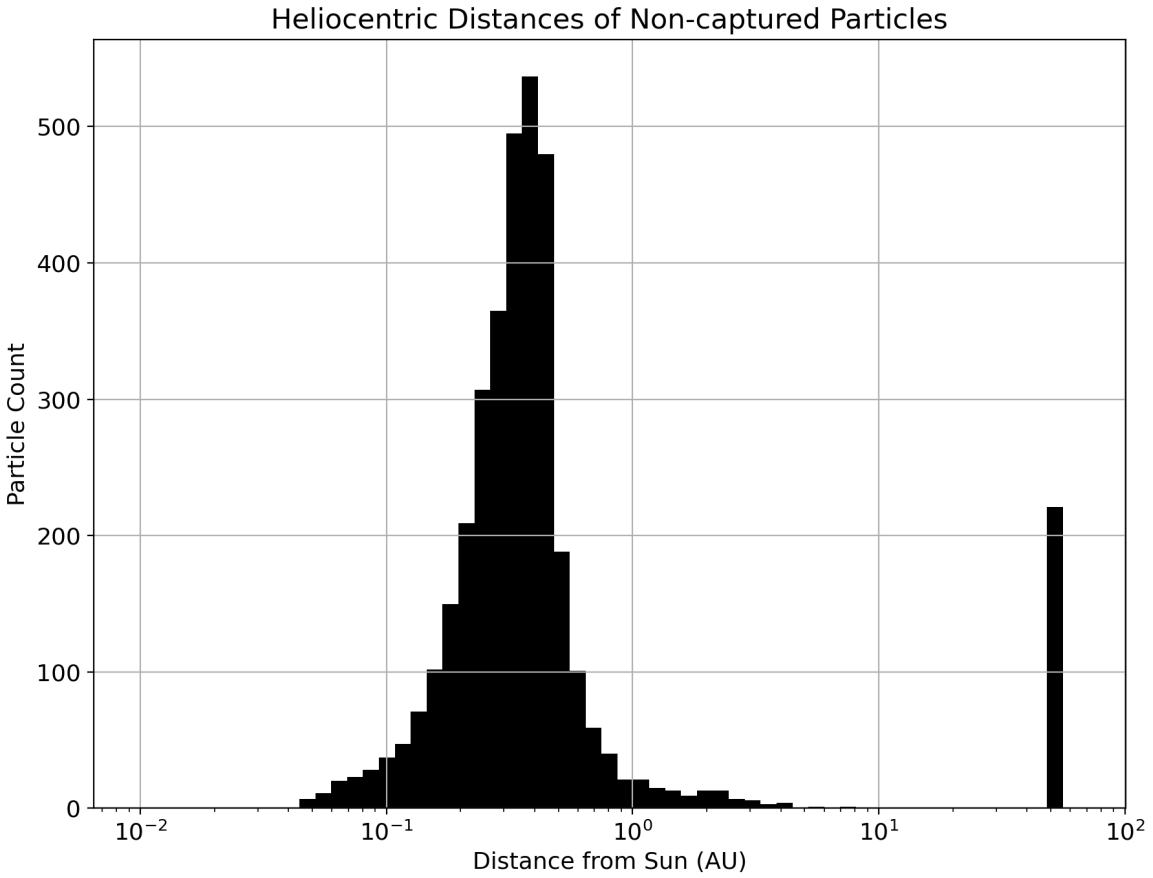

Figure 5.8 The heliocentric distances of all the particles that were not intercepted by the simulations of Sections 5.1-5.5 at the end of the 5000 years of propagation. A majority of the remaining (non-intercepted) particles have stayed at or inside of Mercury's orbit. The peak occurs close to 0.39 AU, the average orbital distance of Mercury. Some particles have moved beyond 1 AU and further into the outer Solar System. Particles that have a heliocentric distance larger than 50 AU are considered to have exited the Solar System. They are represented by the bin at 50 AU.

have migrated beyond 1 AU and a few hundred have escaped the Solar System (have reached a heliocentric distance of greater than 50 AU). Figure 5.8 shows the heliocentric distances of these non-intercepted particles at the end of the 5000 years of propagation.

5.6 Composite Case

The results displayed in this section are from a simulation that incorporates all the previous particle sizes as well as attempting to use all of the impactor-property combinations from Table 4.1. Ideally, that is 240 unique impact cases consisting of 720 separate simulations and a total of 103,680 test particles. All simulations are run for a maximum of 10,000 years. The same

impact model, N-body code, time-step, and Hill sphere radii as the previous simulations are used.

Unfortunately a portion of the simulations were prematurely ended due to factors out of control of the author; sometimes system errors or crashes can occur as well as the occasional maintenance of the supercomputers that ran them. Nearly all simulations were run on Auburn University's *Easley* and *Hopper* supercomputers and these results would not be possible without them. In addition, given the scale of this simulation as well this project's limited time frame, the lost simulations were not able to be recovered. A majority of the lost simulations were the combinations of impact angle, latitude, and longitude of impact while holding impactor radius constant at 1000m. Considering this, the total number of test particles ultimately available for analysis is 98,496. This is still a substantial amount of test particles and data and should still be considered capable of producing meaningful results.

Continuing on, the distribution of particle radii used in this simulation are: 10 μm (50%), 50 μm (40%), 100 μm (5%), 500 μm (4%), and 1000 μm (1%). Motivated by the knowledge that Mercurian regolith is likely smaller, on average, than lunar regolith and as well as values obtained by [78], 90% of the particles are set to 50 μm and smaller with a bias towards the 10 μm particles. As is evident in the results up to this point, the primary consequence of particle size is whether they are more likely to fall into the Sun or return to Mercury (Fig. 5.9a). However, these trends quickly plateau after just reaching 100 μm in size. The other particle capture-properties such as time-to-capture and Hill sphere entrance speed (and subsequently its impact speed) also follow trends with changing particle size, but to a much less pronounced degree (Figs. 5.9b & 5.9c). Thus, the precise percentage of particles at sizes above 100 μm is not as important as the percentages of smaller particles.

With the stated distribution, the average particle radius is 60 μm. If only the 10 μm and 50 μm particles are considered, the average particle radius becomes 27.78 μm. Both of these sizes are within the bounds of [78]'s estimations of lunar and Mercury regolith.

The results of the composite simulation appears as a mix of the 10 μm and 50 μm case, which is what one would expect. Of the total 98,496 test particles, 76,669 (77.84%) were captured. 38,403 (50.09%; 38.99% of total population) returned to Mercury after the 10,000

years propagated (Fig. 5.10). Table 5.1 details the composite simulation by particle size. The percentage of particles that were intercepted for each size are similar to those found in the earlier simulations. They are all slightly greater here because of the longer simulation time which allows for more particles to become captured.

	Sim. Composition		Intercepted by Mercury		
Radius	Particles	Fraction (%)	Particles	Specific Frac. (%)	Total Frac. (%)
10 μm	49,248	50	10,880	22.09	28.33
50 μm	39,399	40	19,894	50.49	51.8
100 μm	4925	5	3381	68.65	8.8
500 μm	3940	4	3376	85.69	8.8
1000 μm	984	1	872	88.62	2.27
Totals	98,496	100	38,403	38.99	100

Table 5.1 Results of composite simulation by particle size. The specific fraction refers to the portion of particles of that size that that returned to Mercury (column 4 / column 2). The total fraction is that size's contribution to the total number of particles that returned to Mercury (column 4 / 38,403).

Not quite as many were captured by the Sun as Mercury, but they are comparable: 32,463 (42.34%; 32.96% of total). Particles were returning to Mercury over the entire time of the simulation, but averaged 861.5 years. A small fraction of particles fell into the Sun almost immediately after ejection, but a majority them were captured after a few thousand years. The average was 5457 years. The average interception velocity for particles at Mercury was 3.28 km s^{-1} which would become an impact speed of 5.34 km s^{-1}. These particles spanned interception velocities from +10 km s^{-1} to -30 km s^{-1} for about 100 years after ejection, but this range began to steadily shrink until it spanned (roughly) ± 5 km s^{-1} at the end of the simulation.

Because of the large number of particles in this case, patterns that were difficult to establish in the previous results are now more clear. For example, at low ejection speeds it follows that those particles are likely to return to Mercury. However, Figure 5.11a makes it clear that Mercury is only the dominant destination for slow moving particles for approximately 5000 years. After this time, particles are much more likely to eventually approach the Sun. In contrast, it can be determined that the more quickly a particle is ejected, the less likely it is to return to Mercury. One could point to Figure 5.10 as evidence for this claim, or the thinning of

points in as ejection velocity increases in Figures 5.11c, 5.11d. However, recall that the amount of 'fast' moving ejecta produced by an impact is always less than the amount of 'slow' moving ejecta (see Fig. 4.3). Thus, the number of fast moving particles available to be captured in the first place will inherently be lower than the amount of slow moving particles (that still escape the planet, of course). Instead, one can argue strictly from a statistical point of view that faster moving ejecta are less likely to return to Mercury because they have access to more planetary bodies. Venus becomes accessible to particles at an ejection speed of $\sim$ 9 km s^{-1}, Earth at $\sim$ 12 km s^{-1}, Mars at $\sim$ 15 km s^{-1}, Jupiter at $\sim$ 18 km s^{-1}, and Saturn at $\sim$ 22 km s^{-1} (Figs. 5.11a, 5.11b, & 5.12a). Therefore, as more planets are now present to potentially capture the fast moving particles, the probability of the particle returning to Mercury must decrease. The importance of establishing these trends is that they ultimately play a role in influencing what percentage of particles will return to Mercury.

Table 5.2 summarizes the numerical results of all of the simulations presented.

		Intercepted Particles (%)			Avg. Time (yrs)		Impact Speed (km s^{-1})
Radius	Q_{pr}	Total	Mercury	Sun	Mercury	Sun	Mercury
10 μm	0.42	85.52	20.54	61.44	493.5	2710	5.43
50 μm	0.38	56.41	46.1	7.28	255	1110	8.66
100 μm	0.42	66.67	62.2	1.82	191	1214	9.22
500 μm	0.60	84.95	80.59	1.19	139	0.064	10.4
1000 μm	0.85	86.51	82.08	1.19	153	0.064	10.44
Composite	–	77.84	38.99	32.96	861.5	5457	5.34

Table 5.2 Summary of the results of the individual particle size simulations and the composite simulation. Percentage of intercepted particles are with respect to the total number in the simulation. Avg. Time refers to the average amount of time after ejection that particles took to be captured by the body. Impact speed is found by accelerating particles down to the surface of Mercury with an initial velocity equal to the velocity at which the particle crossed into the Hill sphere.

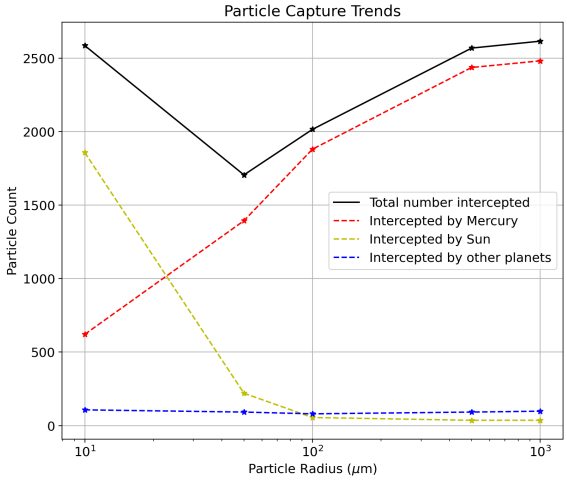

(a) Number of particles intercepted by Mercury, the Sun and the other planets for each particle radius case.

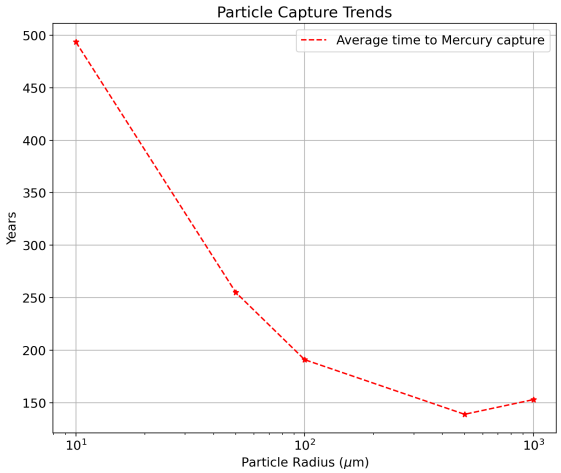

(b) Average amount of time after particle ejection until particles entered Mercury's Hill sphere.

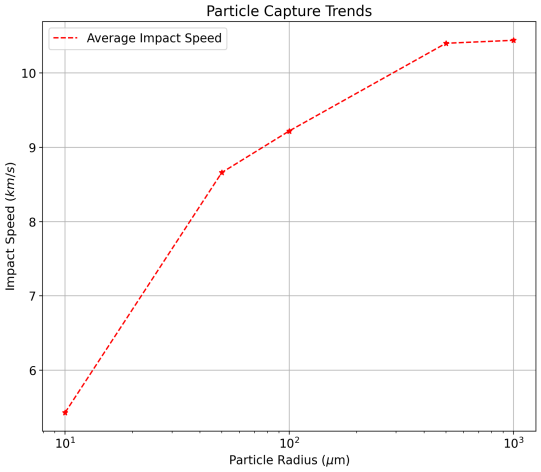

(c) The average impact speeds Mercury returning particles. These values come directly from the particles being accelerated down to Mercury's surface after re-entering its Hill sphere.

Figure 5.9 Trends of intercepted particles based on the individual size simulations from Sections 5.1 to 5.5. At smaller radii, particles are more likely to fall into the Sun rather than return to Mercury as well as re-impact Mercury at lower velocities. However, as radius increases to more than a few 10s of micron, Mercury becomes the dominant destination. At radii larger than 500 micron, the trends of particle interception, time-to-capture, and impact speed begin to stabilize.

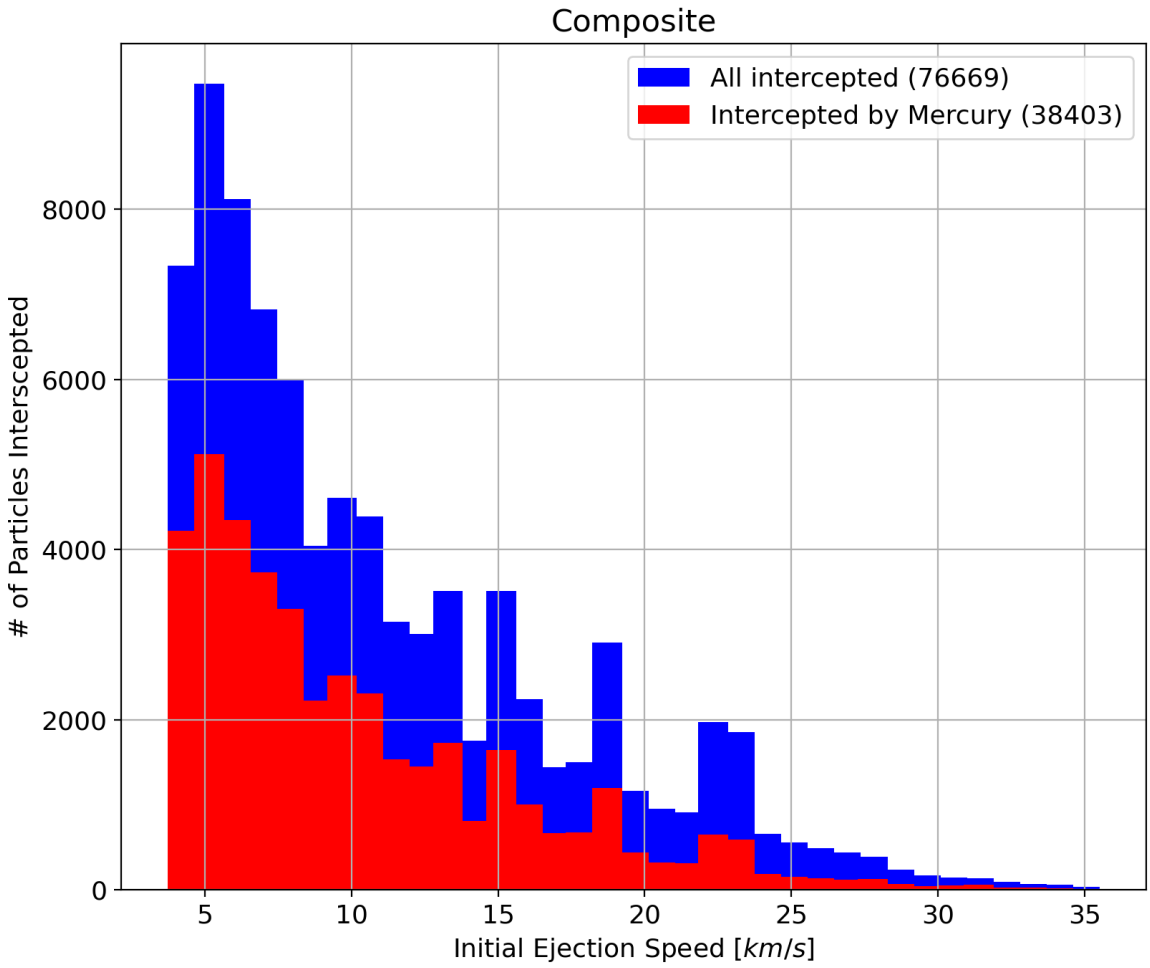

Figure 5.10 Of the 98,496 total particles considered, 76669 (77.84%) were captured (blue). 38,403 particles (50.09% of captured particles; 38.99% of total population) returned to Mercury's Hill sphere (red). As with the previous simulations, faster moving particles are less likely to get intercepted by Mercury or any other body.

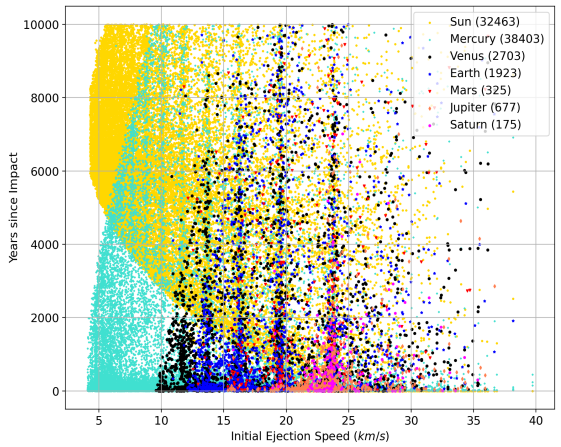

(a) Particle time-to-capture versus launch speed

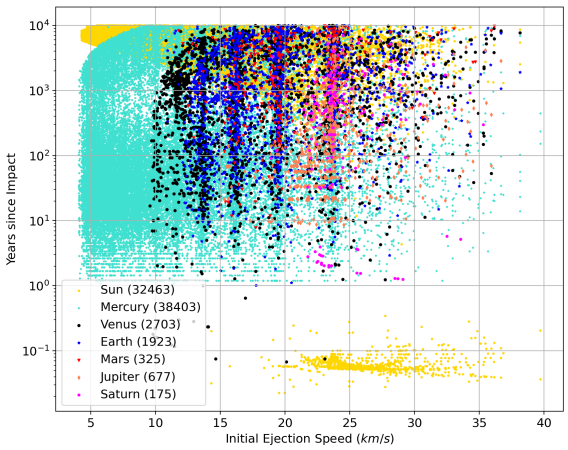

(b) Same as (a), but with logarithmic y-axis

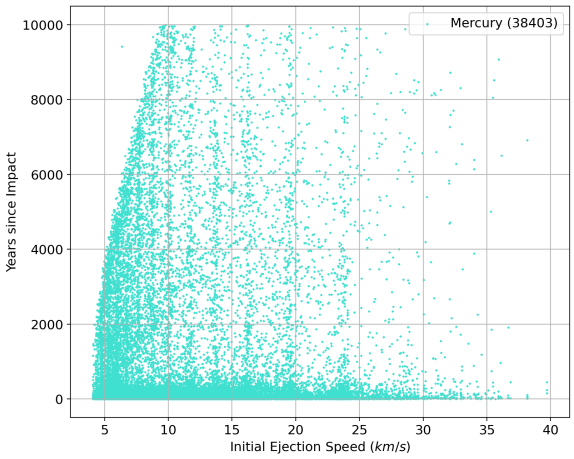

(c) Same as (a), though only displaying Mercury points

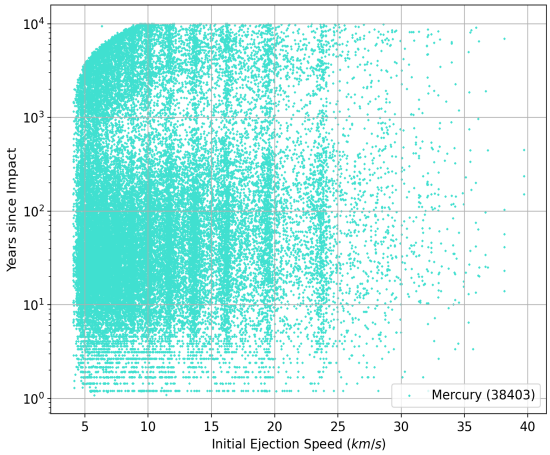

(d) Same as (b), though only displaying Mercury points

Figure 5.11 With more test particles than the previous simulations, distinct regions corresponding to each body becomes apparent. Particles ejected at speeds under 10 km s^{-1} are almost entirely contained to the Sun and Mercury. As ejection speed increases, the particles gain access to interception by more planetary bodies. Planets, including Mercury, will do most of the particle interception for the first 1000 years while the Sun becomes more dominant as time progresses. The subset of Sun-captured particles at the bottom of (b) show that some particles will be nearly immediately swept up by the Sun after ejection and is not an anomaly of individual simulations. This feature is also present in all of the previous results.

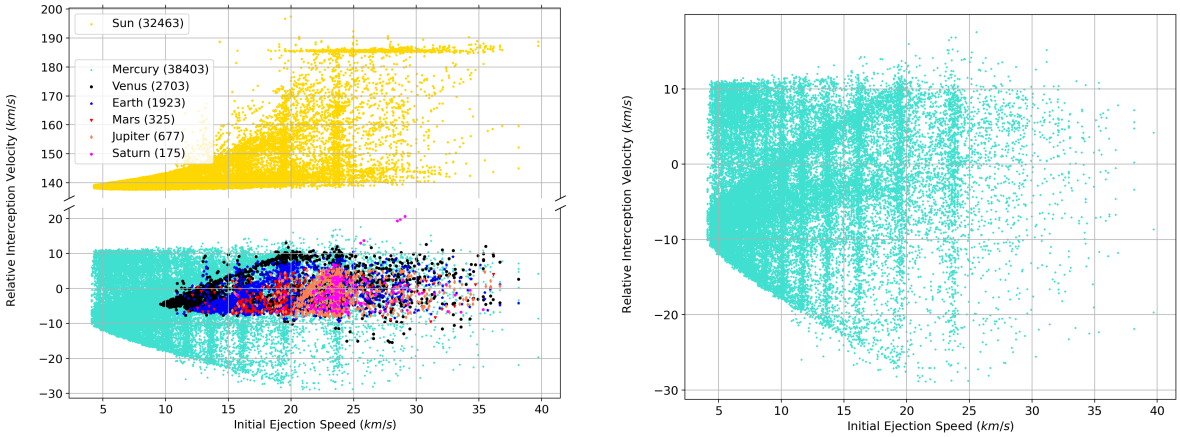

(a) Interception speeds of particles relative to the body that captured them versus launch speed from impact

(b) Same as (a), but only displaying Mercury points.

Figure 5.12 This figure shows the boundaries of what planets are accessible to particles the most clearly. Particles ejected at the full range of velocities can access Mercury and the Sun, which is expected. However, as seen previously, particles with launch speeds in excess of approximately 25 km s^{-1} are much less likely to return to Mercury. Venus becomes accessible at $\sim$ 9 km s^{-1}, Earth at $\sim$ 12 km s^{-1}, Mars at $\sim$ 15 km s^{-1}, Jupiter at $\sim$ 18 km s^{-1}, and Saturn at $\sim$ 22 km s^{-1}. There are particles that can reach each of these planets at ejection speeds below those listed, though these are the speeds at which the bulk of particles must exceed to reach that planet. For all planets besides Mercury, there is a trend that lower the ejection speeds imply lower interception velocities relative to the intercepting planet. Mercury, however, allows particles to maintain interception velocities of ± 10 km s^{-1} at all ejection velocities and as ejection speeds increase, relative interception velocities widen to more negative values, but do not increase to more positive values.

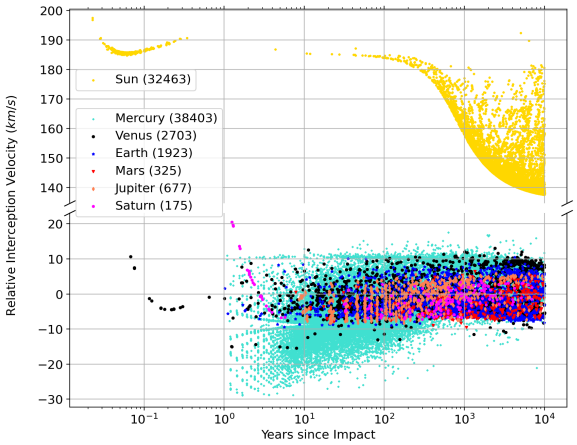

(a) Interception speeds of particles relative to the body that captured them versus time-of-flight

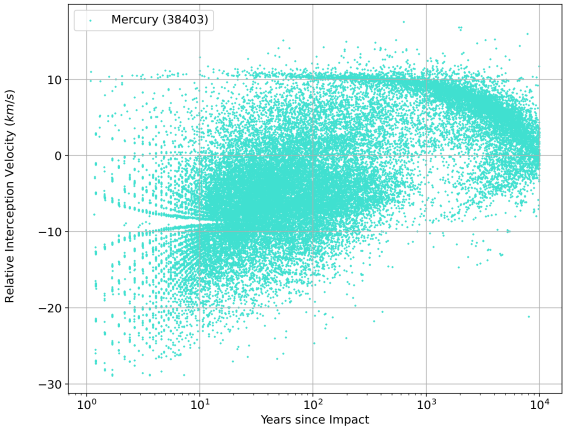

(b) Same as (a), but only displaying Mercury points.

Figure 5.13 Again, with the greater population of particles, noticeable patterns can be discerned. These plots align with those of all the smaller simulations – the particles intercepted by Mercury occupy the same region centered approximately at x = 100 years and y = -10 km s^{-1}. Mercury particles also dominate as the fastest interception velocities (-10 km s^{-1} to -30 km s^{-1}) by planets (i.e. not including Sun-intercepted particles). This makes sense because a negative value of velocity indicates that Mercury 'ran into' the particle. Mercury, having the greatest orbital velocity is more likely to intercept particles at high speeds. This is a part of the reason Mercury has the fastest impact velocity in the Solar System. The Sun also shows the same distinct pattern as seen in the 10 μm case (Fig. 5.1d). This feature is actually present in all the interception-velocity vs. time results, just to a lesser degree. Thus, the trend that as more time passes, particles that fall into the Sun actually begin to get intercepted at lower speeds is not likely to be a property of some select few impact or particle cases.

Chapter 6

Discussion & Conclusions

This final chapter will combine the discussion of the results and the conclusion of the thesis. The discussion aims to further understand the results of the simulations and how they answer this project's primary question of 'how much of Mercury's meteoroid population is composed of material originating from itself?' It will also mention possible shortcoming of this investigation, how it could be improved, and potential future work.

6.1 Discussion of Results

The previous chapter presented the results of a large number of numerical simulations separated into six analyses. Five smaller scale simulations to understand how particle size influences the likelihood of ejecta returning to Mercury and one substantially larger simulation that attempted to more realistically represent material ejected from Mercury. Though it included data on particles captured by other planets, this discussion will primarily focus on particles returning to Mercury and the Sun.

6.1.1 To Return, or Not to Return?

First, the results of the individual particle cases and their implications. Figure 5.9 does a good job summarizing the important information that can be gained from these simulations. The most critical piece of knowledge is visualized in Figure 5.9a. There is a clear relationship between the size of the ejected particles and the likelihood of them returning to Mercury. Particles with radius of 10 μm have a much greater probability of being captured by the Sun rather

than returning to Mercury. Increasing radius to just 50 μm, however, presents a completely different situation where Mercury is by far the dominant particle wrangler. The trend continues with increasing particle size but at a less dramatic rate. This behavior is explained by the non-gravitational perturbations (Eq. (3.35)) influencing orbital trajectories. More specifically, Poynting-Robertson drag causing the 10 μm grains to spiral into the Sun much more rapidly than larger ones.

The Poynting-Robertson effect primarily affects grains with radii of a few micrometers and smaller [80]. A particle's susceptibility to perturbative effects is usually presented as β, the ratio of radiation force to the Sun's gravitational force on the particle [45]:

$$\beta \equiv \frac{F_r}{F_g} = \frac{\left({}^{SA}/_{c}\right) Q_{pr}}{\frac{4}{3}\pi r^3 \rho \left({}^{GM_\odot}/_{x^2}\right)} = \frac{3L_\odot}{16\pi G M_\odot c}\left(\frac{Q_{pr}}{\rho r}\right) = 5.774 \times 10^{-4}\left[\frac{kg}{m^2}\right]\left(\frac{Q_{pr}}{\rho r}\right) \tag{6.1}$$

where $S = {}^{L_\odot}/_{4\pi x^2}$ is the radiation flux density of the Sun at a distance x; $L_\odot$ and $M_\odot$ are the luminosity and mass of the Sun; A, r, and ρ are the cross sectional area, radius, and mass density of the particle, respectively; c is the speed of light; and G is the gravitational constant.

The time it takes, in years, for a particle to spiral from a distance $a_i \rightarrow a_f$ (in AU), and assuming a circular orbit, can then be estimated using the equation [45, 79, 80]

$$\tau_{pr}(yr) = \frac{400}{\beta}\left(a_i^2 - a_f^2\right). \tag{6.2}$$

Table 6.1 presents that values of β for various particle radii as well as τ_{pr} for them to fall from Mercury's average orbital distance to the Sun's effective Hill radius as used in the simulations. The time for a 10 μm particle to migrate inwards this distance is $\sim$ 3700 years. This is on the same order as the average time for grains in the 10 μm particle case to be captured by the Sun (see Table 5.2). τ_{pr} for the 50 μm size increases substantially to $\sim$ 20,000 years which is well beyond the time considered in the simulations. However, the average capture time for the 50 μm particles was found to be only 1110 years. This should not be of much concern, though. Because the number of test particles that fell into the Sun for the 50 μm case decreases to $\sim$ 7% then only $\sim$ 1% of the total population for larger grains, these values are likely

not representative of τ_{pr} for those sizes and is rather a result of small sample size (and short propagation time). In addition, every case had some non-trivial percentage of particles that followed trajectories directly into the Sun (see Fig. 5.2) which is not due to radiative effects, but how the particles are launched from the impact event. This will shift the average time-to-capture to some value below the estimate of τ_{pr}.

The results of the composite case also support this observation. The average time-to-capture for the Sun was 5457 years. Because 50% of the test particles had a radius of 10 μm and 50% had a radius above that, the average value of τ_{pr} should be greater than 3692 years. As propagation time goes to infinity, the average τ_{pr} would gradually increase as more and more larger grains begin to make their way into the Sun. But, the simulations conducted for the composite case terminates at 10,000 years dampening the effect of long-lived grains. Still, one should expect a slight rise in the average τ_{pr} of the composite case because of the presence of the larger particles and longer propagation time.

For the particles with radii greater than 10 μm, they mostly remain in stable orbits near Mercury (see Fig. 5.5) resulting in a much greater return rate. While some fast moving particles do make their way to other planets and the outer solar system, they are too large to be significantly perturbed by solar radiation pressure and blown out of the region around Mercury. Thus, the motion of particles larger than 10 μm are almost entirely governed by gravitational forces.

6.1.2 Mass Return

In number, grains with radius of 500 and 1000 μm make up a small fraction of the regolith ejected from Mercury, but would compose nearly all of the mass. Using the same grain size distribution as the composite simulation, the contribution of each particle size to the total escaped mass (F_r) is:

- 10 μm: $F_{10} = 0.003\%$
- 50 and 100 μm would each contribute $F_{50} = F_{100} = 0.331\%$
- 500μm: $F_{500} = 33.11\%$

Table 6.1. β and τ_{pr} for various particle sizes

Radius	Q_{pr}	β	τ_{pr}(yrs)
0.01 μm*	0.025	0.962	61.4
0.1 μm*	0.16	0.616	95.9
1 μm*	0.78	0.3	196.9
10 μm	0.42	0.016	3692.1
50 μm	0.38	0.0029	2.04×10^4
100 μm	0.42	0.0016	3.7×10^4
500 μm	0.60	0.00046	1.24×10^5
1000 μm	0.85	0.00032	1.85×10^5

Note. — * 0.01, 0.1, and 1 μm are not used in simulations, but are shown here to provide more context for the span of β values. All particles have $\rho = 1500$ kg m^{-3}. τ_{pr} is the time it takes the particle to spiral from Mercury's average orbital distance (0.3871 AU) to the Sun's effective Hill radius ($10R_{\odot}$) assuming a circular orbit.

- 1000 μm: $F_{1000} = 66.223\%$

With this information, the number of particles of each size can be calculated with:

$$P_r = \frac{M_{esc} * F_r}{m_r} \tag{6.3}$$

where P_r is the number of particles of radius r, M_{esc} is the amount of mass launched off the planet (or whatever mass one chooses to analyze), F_r is the fraction of mass contributed by particles with radius r (i.e. $F_{1000} = 0.66223$, $F_{500} = 0.3311$, etc...), and m_r is the mass of a particle with radius r. From this, we can apply the particle return rates found from the simulations to estimate the amount of mass returned to Mercury from an impact event.

As an example, an impactor with radius of 50 meters, velocity of 42 km s^{-1}, and impact angle of 45° should be able to launch $M_{esc} = 6.502 \times 10^5$ kg faster than 4.25 km s^{-1}, according to Eq. (3.32). The number of particles corresponding to each size would be:

- $P_{10} = 3.426 \times 10^{12}$
- $P_{50} = 2.741 \times 10^{12}$
- $P_{100} = 3.426 \times 10^{11}$
- $P_{500} = 2.741 \times 10^{11}$
- $P_{1000} = 6.853 \times 10^{10}$

Finally, using the specific fraction return rate for each particle size (S_{fr}) in column five of Table 5.1, the number of particles for each size and thus, the total mass returning to Mercury, can be estimated:

- $M_{10} = (P_{10}S_{10})m_{10} = (3.426 \times 10^{12} * 0.2209) * 6.283 \times 10^{-12}$ kg $= 5$ kg
- $M_{50} = (P_{50}S_{50})m_{50} = (2.741 \times 10^{12} * 0.5049) * 7.854 \times 10^{-10}$ kg $= 1087$ kg
- $M_{100} = (P_{100}S_{100})m_{100} = (3.426 \times 10^{11} * 0.6865) * 6.283 \times 10^{-9}$ kg $= 1478$ kg
- $M_{500} = (P_{500}S_{500})m_{500} = (2.741 \times 10^{11} * 0.8569) * 7.845 \times 10^{-7}$ kg $= 184,483$ kg

Table 6.2. Fractional makeup of the total ejected mass (F_r) and the fraction of particles of that specific size that return to Mercury (S_{fr})

Radius	m_r (kg)	F_r	S_{fr}
10 µm	6.283×10^{-12}	3×10^{-5}	0.2209
50 µm	7.854×10^{-10}	0.00331	0.5049
100 µm	6.283×10^{-9}	0.00331	0.6865
500 µm	7.854×10^{-7}	0.3311	0.8569
1000 µm	6.283×10^{-6}	0.66223	0.8862

Note. — F_r and S_{fr} here are presented as fractions and not percentages. S_{fr} comes directly from column five of Table 5.1

- $M_{1000} = (P_{1000}S_{1000})m_{1000} = (6.853 \times 10^{10} * 0.8862) * 6.283 \times 10^{-6}$ kg $= 381,581$ kg
- Total mass returning to Mercury: $\sum M_r = 568,634$kg $\Rightarrow 87.45\%$ of escaped mass (6.502×10^5 kg)

Upon closer inspection, this percentage of the original escaped mass returning to Mercury is independent of mass:

$$\frac{M_{return}}{M_{esc}} = \frac{\sum M_r}{M_{esc}} = \sum P_r \frac{S_{fr}m_r}{M_{esc}} = \sum \left(\frac{M_{esc}F_r}{m_r}\right) \frac{S_{fr}m_r}{M_{esc}} = \sum F_r S_{fr} \tag{6.4}$$

So, this percentage is purely a function of the particle size distribution of the regolith (i.e. F_r) and the probability of each grain size to return to the planet (S_{fr}, which itself is heavily influenced by β). These important values are consolidated in Table 6.2 for convenience.

Thus, this study finds that for an impact that can eject regolith faster than Mercury's escape velocity, approximately 40% of escaped ejecta particles composing 87.45% of the escaped mass will return to Mercury over the course of 10,000 years and with an average impact speed of $\sim$ 5.3 km s^{-1}. This has the implication that Mercury's meteoroid environment almost certainly is composed partially of material originating from itself. If unimpeded, these particles will re-impact Mercury's surface and further contribute to surface processes such as boulder

decimation, regolith breakup and gardening, melt production, volatile vaporization and topographic diffusion.

6.2 Potential Improvements and Future Work

This section will list various limitations of this investigation.

To keep the number of simulations to be run to a manageable amount, compromises in possible impact parameters must be made. The two most notable compromises in this project are the decision to consider only one impact velocity and one initial time epoch. The importance of impact velocity to the scaling of impacts is discussed in the earlier chapters. The initial time epoch would influence the orbital evolution of particles and how they interact with the other solar system bodies. However, given that the orbital period of Neptune – the most distant body considered in the simulations – is 165 years and the timescales considered in this project are multiple thousands, all planets are capable of completing a multitude of orbits. This implies that the test particles are subject to the gravity of solar system bodies in a wide range of orientations. Thus, considering multiple initial epochs (during the Solar System's current period of stability), instead of just one, would likely not significantly alter the trends of particle motion on the timescales considered.

On a note related to particle motion over the span of thousands of years, one should typically consider particle collisional lifetimes. That is: over time, interplanetary dust particles tend to collide with other dust particles, further fragmenting them into smaller pieces. The collisional lifetimes for particles depend on their position in the solar system and their mass/size. According to [81] and [44], the collisional lifetimes of the particles with mass $\sim 10^{-12} - 10^{-6}$ kg is on the order of a few thousand years to many tens of thousands of years. Reference [30] emphasizes the importance of a collisional lifetime multiplier F_{coll} for different sized particles and [81] finds that this multiplier becomes important for particles of radii larger than a few hundred micron. Because a majority of the test particles in this project are smaller than 50 micron and maintain orbits near Mercury (~ 0.4 AU), the average collisional lifetime is likely on the order of the timescales of the simulations (5,000 - 10,000 years). The inclusion of a collisional lifetime would further increase the number of small particles, which would ultimately lower the

percentage of particles returning to Mercury. Though, because a majority of the mass returning to Mercury is contained in the 500 μm to 1000 μm size range, and these particles should consider $F_{coll} = 50$ [81], it is unlikely that the percentage of ejecta mass returning would be significantly effected (especially because most of the mass return happens within 1000 years; see Table 5.2).

A final potential shortcoming is that a particle cumulative size-frequency distribution was not used. As discussed earlier, particle size is a strong indicator of if ejecta will return to Mercury or not and the amount of particles with radius larger than 500 μm is the primary source of mass returning to Mercury. Thus, using an actual size distribution of particles would greatly refine the results. Still, the current results of this project should provide meaningful insight into how much material originating from Mercury composes its meteoroid population.

Aside from conducting more simulations, implementing collisional lifetimes, and using a particle size frequency distribution, future work should include simulating impacts on Mercury over the course of millions of years (see [21, 26, 29]) and investigating the equilibrium state (and if there exists an equilibrium) of how much Mercury ejecta is in the meteoroid population at any given time.

6.3 Conclusion

The planet Mercury is subjected to some of the highest velocity impacts in the Solar System. Because it does not have an atmosphere and has a relatively low surface gravity, regolith ejecta only requires meter-sized projectiles to have 18% of the average impact velocity to escape Mercury's Hill sphere (Fig. 4.5). In addition, it also hosts one of the highest cratering rates in the inner Solar System meaning that, on average, Mercury likely expels the most surface material of any major inner Solar System body. This thesis aimed to understand how much of this ejected material will come back to Mercury to contribute to micrometeoroid bombardment, one of the dominant surface processes on Mercury.

Using the ejecta-scaling relationships of Housen & Holsapple (2011) [17] and the particle ejection angle and oblique impact adjustments from Richardson et al. (2007) [32], a suite of impact simulations were conducted to quantify particle ejection velocities. Using the particles'

launch speed and direction, their motion is ballistically propagated until they reach a few hundred kilometers above the surface. They are then transferred to an N-body code that calculates their orbital trajectories for thousands of years under the influence of gravity, solar radiation pressure, and Poynting-Robertson drag. Every particle is monitored for entering into a planetary body's Hill sphere or approaching within 10 solar radii. If a particle enters a Hill sphere or close to the Sun, its orbital trajectory ceases to be propagated. It is assumed that once it enters a Hill sphere, it will eventually impact the surface.

Smaller-scale simulations are first conducted using a few randomly picked impact events (see Table 4.1) and a timescale of 5000 years. These particular cases each only consider a single particle radius to understand how particle size affects the likelihood of returning to Mercury. Radii of 10, 50, 100, 500, and 1000 μm are used. Then, a substantially larger simulation consisting of 98,496 test particles simulated for 10,000 years is performed. For this simulation, the same particle sizes are implemented, but in different amounts: 50% of particles have radius 10 μm, 40% are 50 μm, 5% 100 μm, 4% 500 μm, and 1% 1000 μm. This distribution is interpreted from the findings that Mercury regolith likely has an average radius of 22^{+46}_{-18} μm [78].

The 50, 100, 500, and 1000 μm particles were all found to return to Mercury at high rates. These particles are not appreciably perturbed by non-gravitational forces. On the other hand, 10 μm particles re-entered Mercury's Hill sphere less frequently. This is due to the more pronounced decelerating effect Poynting-Robertson drag has on smaller particles. An estimation of the time it takes a 10 μm particle to spiral into the Sun from the orbit of Mercury is in agreement with our results of the average time-to-capture by the Sun for these sized grains. Mercury is the dominant terminus for grains 50 micron and larger. The Sun dominates the 10 micron particles. As a general trend, the larger the particle, the more likely it will return. It was also found that the larger the grain, the higher its impact velocity will be.

Overall, this study estimates that approximately 39% of particles and 87% of mass that escapes Mercury via an impact event will return on astronomically short time scales. A major portion of this ejecta is on the order of a few 10s of microns and, by number, will make up about 80% of returning particles but only 0.2% of returned mass. Alternatively, particles with

radii greater than a few hundreds of micron compose less than 20% of particles returning to Mercury, but over 99.5% of the returning mass. The fraction of the total escaped mass that comes back to Mercury is independent of mass and relies only on the particle size distribution of the ejecta and the rates at which each grain size returns to Mercury.

Mercury's meteoroid population is likely to consist of material ejected off of the planet via impact. Such material can re-impact and play a role in surface alteration processes such as boulder decimation, regolith breakup and gardening, melt production, volatile vaporization and topographic diffusion.

References

[1] Borin, P., Cremonese, G., & Marzari, F. (2016) "Statistical analysis of the flux of micrometeoroids at Mercury from both cometary and asteroidal components." *A&A*, 585, A106

[2] Borin, P., Cremonese, G., Marzari, F., Bruno, M., & Marchi, S. (2009) "Statistical analysis of micrometeoroids flux on Mercury." *A&A*, 503, 259

[3] Cintala, M. J., Berthoud, L., & Hörz, F. (1999) "Ejection-velocity distributions from impacts into coarse-grained sand." *Meteoritics & Planetary Science*, 34, 605

[4] Cintala, M. J. (1992) "Impact-Induced Thermal Effects in the Lunar and Mercurian Regolith." *Journal of Geophysical Research*, 97, E1

[5] Domingue, D., Chapman, C., Killen, R., et al. (2014) "Mercury's Weather-Beaten Surface: Understanding Mercury in the Context of Lunar and Asteroidal Space Weathering Studies." *Space Science Reviews*, 181, 121

[6] Cremonese, G., Bruno, M., Mangano, V., Marchi, S., & Milillo, A. (2005) "Release of neutral sodium atoms from the surface of Mercury induced by meteoroid impacts." *Icarus*, 177, 1

[7] Fassett, C. I., Kadish, S. J., Head, J. W., Solomon, S. C., & Strom, R. G. (2011) "The global population of large craters on Mercury and comparison with the Moon." *Geophys. Res. Lett.*, 38, 10

[8] Granvik, M., Morbidelli, A., Jedicke, R., et al. (2018) "Debiased orbit and absolute-magnitude distributions for near-Earth objects." *Icarus*, 312, 181

[9] Vaniman, D. T., Reedy, R., Heiken, G., et al. (1991) in "Lunar Sourcebook: A User's Guide to the Moon." ed. Heiken, G. H., Vaniman, D. T., & French, B. M., *Cambridge University Press*, 27

[10] Hörz, F., Grieve, R., Heiken, G., et al. (1991) in "Lunar Sourcebook: A User's Guide to the Moon." ed. Heiken, G. H., Vaniman, D. T., & French, B. M., *Cambridge University Press*, 61

[11] McKay, D. S., Heiken, G., Basu, A., et al. (1991) in "Lunar Sourcebook: A User's Guide to the Moon." ed. Heiken, G. H., Vaniman, D. T., & French, B. M., *Cambridge University Press*, 285

[12] Carrier III, D. W., Olhoeft, G. R., Mendell, W. (1991) in "Lunar Sourcebook: A User's Guide to the Moon." ed. Heiken, G. H., Vaniman, D. T., & French, B. M., *Cambridge University Press*, 475

[13] Rubin, A. E., & Grossman, J. N. (2010) "Meteorite and meteoroid: New comprehensive definitions." *Meteoritics & Planetary Science*, 45, 1

[14] Housen, K. R., Schmidt, R. M., & Holsapple, K. A. (1983) "Crater Ejecta Scaling Laws: Fundamental Forms Based on Dimensional Analysis." *Journal of Geophysical Research*, 88, B3 (1983)

[15] Holsapple, K. A. & Schmidt, R. M. (1987) "Point Source Solutions and Coupling Parameters in Cratering Mechanics." *Journal of Geophysical Research*, 92, B7

[16] Holsapple, K. A. (1993) "The scaling of impact processes in planetary sciences." *Annual Review of Earth and Planetary Sciences*, 21, 333

[17] Housen, K. R., & Holsapple, K. A. (2011) "Ejecta from impact craters." *Icarus*, 211, 856

[18] Housen, K. R. (2003) in Lunar and Planetary Science Conference, ed. S. Mackwell & E. Stansbery. "Material Motions and Ejection Velocities for Impacts in Porous Targets." *Lunar and Planetary Science Conference*, 1300

[19] Holsapple, K. A. (2009) "On the 'strength' of the small bodies of the solar system: A review of strength theories and their implementation for analyses of impact disruptions." *Planetary and Space Science*, 57, 127

[20] Le Feuvre, M., & Wieczorek, M. A. (2008) "Nonuniform cratering of the terrestrial planets." *Icarus*, 197, 291

[21] Le Feuvre, M., & Wieczorek, M. A. (2011) "Nonuniform cratering of the Moon and a revised crater chronology of the inner Solar System." *Icarus*, 214, 1

[22] Li, R., Zhou, G., Yan, K., & Chen, J. (2021) "Preparation and characterization of a specialized lunar regolith simulant for use in lunar low gravity simulation." *International Journal of Mining Science and Technology*

[23] Liu, X., & Schmidt, J. (2018) "Dust arcs in the region of Jupiter's Trojan asteroids." *A&A*, 609, A57

[24] Maxwell, D. E. (1977) "Simple Z model for cratering, ejection, and the overturned flap" in Impact and Explosion Cratering: Planetary and Terrestrial Implications. *Pergamon Press (NY)*, 1003-1008

[25] Marchi, S., Chapman, C. R., Fassett, C. I., et al. (2013) "Global resurfacing of Mercury 4.0–4.1 billion years ago by heavy bombardment and volcanism." *Nature*, 499, 59

[26] Marchi, S., Mottola, S., Cremonese, G., Massironi, M., & Martellato, E. (2009) "A New Chronology for the Moon and Mercury." *The Astronomical Journal*, 137, 4936

[27] Melosh, H. J. (1989) "Impact Cratering: A Geologic Process." *Oxford University Press*

[28] Barnouin, O. S., Zuber, M. T., Smith, D. E. et al. (2012) "The morphology of craters on Mercury: Results from MESSENGER flybys." *Icarus*, 219. 414

[29] Neukum, G., Oberst, J., Hoffmann, H., Wagner, R., & Ivanov, B. A. (2001) "Geologic evolution and cratering history of Mercury." *Planetary and Space Science*, 49, 1507

[30] Pokornỳ, P., Sarantos, M., & Janches, D. (2018) "A comprehensive model of the meteoroid environment around Mercury." *The Astrophysical Journal*, 863, 31

[31] Richardson, J. E., & Abramov, O. (2020) "Modeling the formation of the lunar upper megaregolith layer." *The Planetary Science Journal*, 1, 2

[32] Richardson, J. E., Melosh, H. J., Lisse, C. M., & Carcich, B. (2007) "A ballistics analysis of the Deep Impact ejecta plume: Determining Comet Tempel 1's gravity, mass, and density." *Icarus*, 191, 176

[33] Solomon, S. C., McNutt Jr, R. L., Gold, R. E., et al. (2001) "The MESSENGER mission to Mercury: Scientific objectives and implementation." *Planetary and Space Science*, 49, 1445

[34] Zharkova, A. Y., Kreslavsky, M. A., Head, J. W., & Kokhanov, A. A. (2021) "Regolith textures on Mercury: Comparison with the Moon." *Icarus*, 351, 113945

[35] Zharkova, A. Y., Kreslavsky, M. A., et al. (2015) "Morphometry of small flat floored craters on Mercury: implications for regolith thickness." *American Geophysical Union Fall Meeting*, Abstract P53A-2099

[36] Poppe, A. R. (2016) "An improved model for interplanetary dust fluxes in the outer Solar System." *Icarus*, 264, 369

[37] Wisdom, J. & Holman, M. (1991) "Symplectic maps for the N-body problem." *The Astronomical Journal*, 102, 1528

[38] Levison, H. F. & Duncan, M. J. (1994) "The Long-Term Dynamical Behavior of Short-Period Comets." *Icarus*, 108, 18

[39] Gladman, B., Duncan, M. & Candy, J. (1991) "Symplectic integrators for long-term integrations in celestial mechanics." *Celestial Mechanics and Dynamical Astronomy*, 52, 221

[40] Chen, Z. & Tan, D. (2012) “On A General Formula of Fourth Order Runge-Kutta.” *Journal of Mathematical Sciences Mathematics Education*, 7, 2

[41] England, R. (1969) “Error estimate for Runge-Kutta type solutions of ordinary differential equation.” *The Computer Journal*, 12, 166

[42] Chambers, J. E. (1999) “A hybrid symplectic integrator that permits close encounters between massive bodies.” *MNRAS*, 304, 793

[43] Borin, P., Cremonese, G., Marzari, F., & Lucchetti, A. (2017) “Asteroidal and cometary dust flux in the inner solar system.” *A&A*, 605, A94

[44] Grün, E., Zook H. A., Fechtig H., & Giese R. H. (1985) “Collisional balance of the meteoritic complex.” *Icarus*, 62, 244

[45] Burns, J. A., Lamy P. L., & Soter, S. (1979) “Radiation forces on small particles in the solar system.” *Icarus*, 40, 1

[46] Morbidelli, A. (2002) “Modern Celestial Mechanics : Aspects of Solar System Dynamics.” Taylor & Francis, London

[47] Byrne, P. K., Ostrach, L. R., et al. (2016) “Widespread effusive volcanism on Mercury likelyended by about 3.5 Ga.” *Geophys. Res. Lett.*, 43, 7408

[48] Thomas, R. J. & Rothery, D. A. (2019) “Volcanism on Mercury.” *Elements*, 15, 1

[49] Fassett, C. I., Crowley, et al. (2017) “Evidence for rapid topographic evolution and crater degradation on Mercury from simple crater morphometry.” *Geophys. Res. Lett.*, 44, 5326

[50] Jasinski, J. M., Regoli, L. H., et al. (2020) “A transient enhancement of Mercury’s exosphere at extremely high altitudes inferred from pickup ions.” *Nature Communications*, 11, 4350

[51] Killen, R., Cremonese,G., et al. (2007) “Processes that Promote and Deplete the Exosphere of Mercury.” *Space Sci. Rev.*, 132, 433

[52] Kobayashi, M., Shibata, H., et al. (2020) “Mercury Dust Monitor (MDM) Onboard the Mio Orbiter of the BepiColombo Mission.” *Space Sci. Rev*, 216, 144

[53] Pokorný, P., Mazarico, E., & Schorghofer, N. (2021) “Erosion of Volatiles by Micrometeoroid Bombardment on Ceres and Comparison to the Moon and Mercury.” *The Planetary Science Journal*, 2, 85

[54] Deutsch, A. N., Head J. W., & Neumann, G. A. (2020) “Analyzing the ages of south polar craters on the Moon: Implications for the sources and evolution of surface water ice.” *Icarus*, 336, 113455

[55] Hirabayashi, M., Howl, B. A., et al. (2018) “The Role of Breccia Lenses in Regolith Generation From the Formation of Small, Simple Craters: Application to the Apollo 15 Landing Site.” *Journal of Geophysical Research: Planets*, 123, 527

[56] Marchi, S., Morbidelli, A., & Cremonese, G. (2005) “Flux of meteoroid impacts on Mercury.” *A&A*, 431, 1123

[57] Marchi, S., Massironi, M., et al. (2011) “The effects of the target material properties and layering on the crater chronology: the case of Raditladi and Rachmaninoff basins on Mercury.” *Planetary and Space Science*, 59, 1968

[58] Poppe, A. R., Lisse, C. M., et al. (2019) “Constraining the Solar System’s Debris Disk with In Situ New Horizons Measurements from the Edgeworth–Kuiper Belt.” *ApJL*, 881, L12

[59] Jewitt, D. C. (2002) “From Kuiper Belt Object to Cometary Nucleus: The Missing Ultrared Matter.” *The Astronomical Journal*, 123, 1039

[60] Kreslavsky, M. A., Zharkova, A. Y., Head, J. W., & Gritsevich, M. I. (2021) “Boulders on Mercury.” *Icarus*, 369, 114628

[61] Kreslavsky, M. A. & Head, J. W. (2015) “A Thicker Regolith on Mercury.” *Lunar and Planetary Science Conference XLVI*, 1246

[62] Cassidy, T. A., Schmidt, C. A., et al. (2021) “Detection of Large Exospheric Enhancements at Mercury due to Meteoroid Impacts.” *The Planetary Science Journal*, 2, 175

[63] Leblanc, F., Schmidt, C., et al. (2022) “Comparative Na and K Mercury and Moon Exospheres.” *Space Science Reviews*, 218, 2

[64] Burger, M. H., Killen, R. M. et al. (2014) “Seasonal variations in Mercury’s dayside calcium exosphere.” *Icarus*, 238, 51

[65] Buckingham, E. (1914) “On Physically Similar Systems; Illustrations of the Use of Dimensional Equations.” *Physical Review*, 4, 4

[66] Baker W. E., Westine, P.S., & Dodge, F.T., editors. (1991), 2 - Development of Model Laws from the Buckingham Pi Theorem in “Similarity Methods in Engineering Dynamics.” *Elsevier*, Fundamental Studies in Engineering, 12, 19-31

[67] Jackson, P. M., Nakano, R., Kim, Y., & Hirabayashi, M. (2022) “Active Main-belt Asteroid (6478) Gault: Constraint on Its Cohesive Strength and the Fate of Ejected Particles in the Solar System.” *The Planetary Science Journal*, 3, 16

[68] Cline II, C. J. & Cintala, M. J. (2022) “Evidence of High-Angle Ejecta From Impacts into Various Granular Materials.” *Lunar and Planetary Science Conference LIII*, 1090

[69] Morbidelli, A., & Gladman, B. (1998) “Orbital and temporal disributions of meteorites originating in the asteroid belt.” *Meteoritics & Planetary Science*, 33, 999

[70] Holsapple, K. A., & Housen, K. R. (2007) “A crater and its Ejecta: An Interpretation of Deep Impact.” *Icarus*, 187, 345

[71] Housen, K. R., Sweet, W. J, & Holsapple, K. A. (2018) “Impacts into porous asteroids.” *Icarus*, 300, 72

[72] Zahnle, K., Alvarellos, J. L., Dobrovolskis, A., & Hamill, P. (2008) “Secondary and sesquinary craters on Europa.” *Icarus*, 194, 660

[73] Singer, K. N., McKinnon, W. B., Nowicki, L. T. (2013) “Secondary craters from large impacts on Europa and Ganymede: Ejecta size–velocity distributions on icy worlds, and the scaling of ejected blocks.” *Icarus*, 226, 865

[74] Singer, K. N., Jolliff, B. L., & McKinnon, W. B. (2020) “Lunar Secondary Craters and Estimated Ejecta Block Sizes Reveal a Scale-Dependent Fragmentation Trend.” *Journal of Geophysical Research: Planets*, 125, 8

[75] Langevin, Y. (1997) “The regolith of Mercury: present knowledge and implications for the Mercury Orbiter mission.” *Planetary and Space Science*, 45, 1

[76] Carrier III, W. D. (2003) “Particle Size Distribution of Lunar Soil.” *Journal of Geotechnical and Geoenvironmental Engineering*, 129, 10

[77] Carrier III, W. D. (2005) “The Four Things You Need to Know About the Geotechnical Properties of Lunar Soil.”

[78] Gundlach, B., & Blum, J. (2013) “A new method to determine the grain size of planetary regolith.” *Icarus*, 223, 1

[79] Klačka, J. & Kocifaj, M. (2008) “Times of inspiralling for interplanetary dust grains.” *MNRAS*, 390, 4

[80] Leinert, C. & Grün, E. (1990) “Interplanetary Dust.” in Schewenn, R. & Marsch, E., eds. “Physics of the Inner Heliosphere I.” *Springer-Verlag*, Berlin, 207

[81] Soja, R. H., Grün, E., et al. (2019) “IMEM2: a meteoroid environment model for the inner solar system.” *Astronomy & Astrophysics*, 628, A109